Boundary-Layer and Low-Level Moisture Fluxes during Low-Level Jet Events in South China and Their Relationship with Early Summer Rainfall

Lin Su,[a,b] Junhao Hu,[a,b] Yu Du,[a,b] Junlu Li,[c] and Guixing Chen[a,b]

[a] School of Atmospheric Sciences, Sun Yat-sen University and Southern Marine Science and Engineering Guangdong Laboratory (Zhuhai), Zhuhai, China
[b] Key Laboratory of Tropical Atmospheric-Ocean System, Ministry of Education, Zhuhai, China
[c] School of Marine Sciences, Sun Yat-sen University, Zhuhai, China

(Manuscript received 16 September 2023, in final form 19 December 2024, accepted 10 January 2025)

ABSTRACT: Low-level jets (LLJs) play a key role in driving early summer rainfall in South and East China (SEC) by supplying essential moisture and energy for convective processes. LLJs in South China (SC) are classified into two distinct types: synoptic-system-related LLJ (SLLJ) and boundary layer jet (BLJ), each exerting distinct influences on rainfall mechanisms. This study investigates the individual influence of SLLJ and BLJ, as well as their interplay, on early summer rainfall over SEC, with a focus on moisture flux dynamics. The findings reveal the independent yet equally significant contributions of SLLJs and BLJs in shaping the pattern of early summer rainfall in SEC. Rainfall intensity over SEC correlates with the intensity of BLJs. Strong BLJs result in pronounced boundary layer convergence and upward moisture transport, and thus favorable for enhanced rainfall over SEC. The location of rainfall is closely associated with the pattern of SLLJs. Southwesterly SLLJs along the coast of SC enhances local low-level convergence and upward motions, leading to rainfall mainly confined to SC. By contrast, a quasi-meridional-oriented SLLJ promotes the low-level northward advection of moisture, which is elevated from the boundary layer by topography in SC. This part of moisture, along with the northward-transported moisture within the boundary layer, is elevated to upper layers at the frontal zone in East China (EC), jointly contributing to enhanced rainfall in EC. Overall, the moisture for rainfall in SC is mainly contributed by the transport of BLJs, whereas the moisture for rainfall in EC is jointly attributed to the northward moisture advection by both BLJs and SLLJs.

SIGNIFICANCE STATEMENT: Low-level jets (LLJs) are frequently observed in South China (SC) during warm seasons and play a key role in early summer rainfall over the region by providing the moisture and energy necessary for convective processes. LLJs in the coastal south and continental China are classified into two types: synoptic-system-related LLJ (SLLJ) and boundary layer jet (BLJ), each exerting distinct influences on rainfall mechanisms. Despite their distinct characteristics and impacts on rainfall, the influences of SLLJs and BLJs on rainfall pattern are interconnected with each other through their interactions. In this work, an in-depth study considering the boundary layer and low level as a whole is conducted to fully understand not only the individual role of SLLJs and BLJs but also their interaction in shaping the spatial pattern of early summer rainfall in South and East China (SEC). The results reveal the distinct yet equally crucial roles of SLLJs and BLJs in determining the location and intensity of early summer rainfall over SEC in a climatological manner and underscore the need for further investigation to quantitatively understand the individual and interactive influences of SLLJs and BLJs on early summer rainfall across various SEC regions.

KEYWORDS: Jets; Rainfall; Moisture/moisture budget

1. Introduction

A low-level jet (LLJ) is referred to a narrow airflow found in the lowest few kilometers of the atmosphere (Bonner 1968; Stensrud 1996). LLJs are the result of temperature gradients, which subsequently induce a pressure gradient and a corresponding flow of air perpendicular to that gradient. Therefore, LLJs predominantly occur in regions with significant thermal contrast often brought about by large-scale topography or land–sea contrast, such as the U.S. Great Plains (Helfand and Schubert 1995; Whiteman et al. 1997), South America (Marengo et al. 2002; Vera et al. 2006), East Africa (King et al. 2021; Munday et al. 2021), and southeast China (Cui et al. 2023; Du and Chen 2019a). LLJs are known to be important to the rainfall in these regions as they carry abundant warm and moist air originated from the tropical oceanic surface (Higgins et al. 1997; Monaghan et al. 2010; Stensrud 1996). LLJs influence rainfall through providing thermal and dynamic conditions conducive to convections. LLJs induce positive vorticity (Beebe and Bates 1955; Walters and Winkler 2001) and mass convergence (Xia et al. 2006; Xia and Zhao 2009; Zhang and Ni 2009) along the left side of their axes, making the region preferred for heavy rainfall occurrences. In addition, LLJs can trigger convections in the regions of their exits by producing low-level convergence and upward motion through their interactions with local land–sea contrast and terrains (Du et al. 2020a; Higgins et al. 1997; Liu et al. 2014).

Numerous studies have revealed that LLJs are frequently observed in South China (SC) during warm seasons and play a key role in early summer (May–July) rainfall over SC and

---

Corresponding authors: Lin Su, sulin8@mail.sysu.edu.cn; Guixing Chen, chenguixing@mail.sysu.edu.cn

DOI: 10.1175/JCLI-D-23-0561.1

East China (EC) by providing the moisture and energy necessary for convective processes (Du and Chen 2019a; Luo 2017). Annually, the most intensive rainfall period in South and East China (SEC), including the presummer (May–June) rainfall in SC and the mei-yu (June–July) in EC, is closely linked to the activities of LLJs. According to the previous studies, approximately 70% of the presummer heavy rainfall events in coastal SC are associated with LLJs (Li and Du 2021); 84% likelihood that a heavy rainfall event will begin on the next day in the region from EC to Japan when there is a LLJ of at least 12.5 m s^{-1} present at 700 hPa (Chen and Yu 1988); and in the Yangtze River valley, 79% of LLJs are accompanied by heavy rainfall during the mei-yu season, and 83% of heavy rainfall events are associated with LLJs (Wang et al. 2003; Wang et al. 2019).

In recent studies, LLJs in the coastal south and continental China are further classified into two types: synoptic-system-related LLJs (SLLJs) and boundary layer jets (BLJs), based on their characteristics and formation mechanisms (Cui et al. 2023; Du and Chen 2019a; Du et al. 2022, 2012, 2014, 2020a; Zhang and Meng 2019; Zhang et al. 2022). SLLJs form in response to synoptic weather systems and usually appear at 850–700 hPa, stretching from the South China Sea to inland SC (Chen and Yu 1988; Du and Chen 2019a; Du et al. 2014). In contrary, BLJs occur within boundary layer over the northern SCS, with a nocturnal wind maximum at 950 hPa (Du and Chen 2019a; Du et al. 2022; Li and Du 2021). SLLJs and BLJs affect rainfall through different mechanisms. The former is more associated with rainfall in inland areas through interaction with synoptic systems to the north, whereas the latter is closely related to coastal rainfall through their intensive interaction with local conditions (Du and Chen 2019a; Du et al. 2022; Li and Du 2021; Zhang and Meng 2019). Particularly, the simultaneous coexistence of a SLLJ and a BLJ favors the formation of coastal convections arising from low-level convergence induced by BLJ and midlevel divergence caused by SLLJ (Du and Chen 2019b; Huang et al. 2022; Liu et al. 2020). These two types of LLJs also differ in moisture transport (Du and Chen 2019a), which influences accumulated rainfall (Chen et al. 2017). There is preferential moisture transport to the coastal rainfall by BLJs and to the inland rainfall by the elevated SLLJs (Du and Chen 2019a).

Despite their distinct characteristics and impacts on rainfall, the influences of SLLJs and BLJs on rainfall pattern are interconnected with each other through their interactions. Most previous studies to date have focused on the respective role of either SLLJs or BLJs in modulating rainfall pattern by separating the two completely; however, BLJ and SLLJ occur simultaneously at a lot of time. In addition, different configurations of the location, direction, and intensity of BLJ and SLLJ may affect regional rainfall in different ways, to which limited attention has been paid. An in-depth study considering the boundary layer and low level as a whole is needed to fully understand not only the individual role of SLLJs and BLJs but also their interaction in shaping the spatial pattern of early summer rainfall in SEC. By utilizing a long-term rain gauge record of rainfall in China and an atmospheric reanalysis dataset spanning from 1976 to 2015 in this study, we investigate the characteristics of different configurations of SLLJs and BLJs in SEC with a particular focus on moisture flux dynamics and further discuss their relationship with the spatial patterns of early summer rainfall over the region. From a perspective of moisture transport, this work is designed to address two key scientific questions: 1) how does the early summer rainfall pattern in SEC response to changes in boundary layer and low-level moisture flux due to varying configurations of location, direction, and intensity of LLJs? and 2) what are the roles of horizontal/vertical moisture transports corresponding to different configurations of LLJs in modulating the spatial pattern of early summer rainfall in SEC? By answering these questions, we aim to provide a more comprehensive understanding of the intricate roles and interactions of SLLJs and BLJs in shaping rainfall patterns in SEC. The remainder of the manuscript is organized as follows: the data used for the study are introduced in section 2, the method applied to the study is described in details in section 3, the results are presented and discussed in sections 4 and 5, and the conclusions are given in section 6.

2. Data

a. Rainfall observations

The annual early summer (1 May–31 July) rainfall in SEC, with a range of 18°–31°N, 107°–124°E (Luo et al. 2020; Zhang et al. 2011) as demonstrated in Fig. 1, is derived from the rain gauge record of daily rainfall at 410 stations across the region. The station locations are depicted in Fig. 1a, and the mean early summer rainfall during 1976–2015 at each station is presented in Fig. 1b. Overall, the mean early summer rainfall in SEC shows two primary centers. One is situated in SC, specifically below 25°N (highlighted by the red box in Fig. 1a), with the heaviest rainfall primarily concentrated along the coast of SC; the second center is found in EC, which is to the north of 25°N and the east of 114°E (indicated by the green box in Fig. 1b); and the most significant rainfall is located at the lower reaches of the Yangtze River. These two rainfall centers correspond to the presummer rainfall period in SC from May to June, and the mei-yu period in EC from June to July, respectively.

b. Atmospheric reanalysis

The fifth major global reanalysis produced by the European Centre for Medium-Range Weather Forecasts (ERA5) dataset with a horizontal resolution of 0.25° at a time interval of 1 h are used for the identification of LLJs in SC and calculation of associated moisture fluxes. The ERA5 combines great amounts of historical observations into global estimates using advanced modeling and data assimilation systems (Hersbach et al. 2020) and has been reported to perform markedly better compared to its coarser-resolution predecessors (He et al. 2021; Q. Jiang et al. 2021; Y. Jiang et al. 2021; Guo et al. 2021; L. Liu et al. 2021; Song and Wei 2021). A number of studies have been conducted to comprehensively examine the applicability of the ERA5 in representing historical

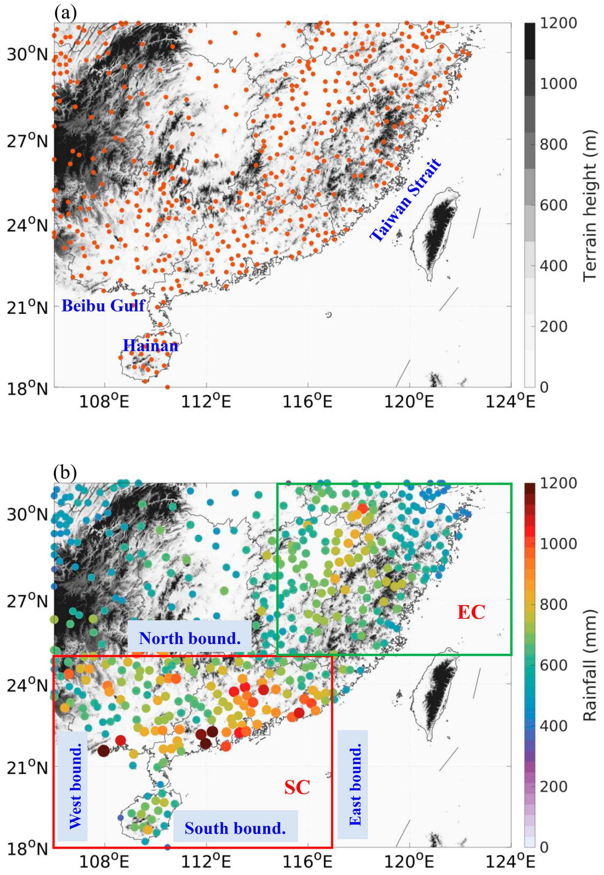

FIG. 1. Topography of SEC with (a) the location of the weather stations used in this study and (b) annual early summer rainfall at the stations over SC; the red box indicates SC; and the green box indicates EC.

meteorological fields, including temperature (Chao et al. 2020; Tang et al. 2021; Zou et al. 2022), wind (Chen et al. 2021; Y. Jiang et al. 2021; Guo et al. 2021), moisture (W. Zhang et al. 2019; Y. Zhang et al. 2019), and precipitation fields (Q. Jiang et al. 2021; Jiao et al. 2021; Wu et al. 2022; Xie et al. 2022) in China. These studies demonstrate a good performance of the ERA5 in reproducing the spatiotemporal variability in meteorological fields across most regions of China and even outperform satellite retrievals in some circumstances or regions.

3. Method

a. LLJ identification

The criteria described in Du et al. (2014) and Du and Chen (2019a) are utilized to identify LLJ events in SC. The region applied to LLJ identification is consistent with the domain of SC (indicated by the red box in Fig. 1b). Based upon the 1-h ERA5 data, a LLJ exists at a grid if the following two conditions are fulfilled: the maximum wind speed at the grid is larger than 10 m s^{-1} below 700 hPa and the difference between the wind maximum and the wind minimum from above the level of wind maximum to 600 hPa is at least 3 m s^{-1}. If the wind maximum is detected below 900 hPa and it is southerly (with positive v components), the LLJ is identified as a BLJ event, else if the wind maximum is detected above 900 hPa and it is southwesterly (with positive u and v components), it is a SLLJ event. A BLJ (SLLJ) event over SC is defined if BLJ (SLLJ) occurs at over 15% grid points over SC at a specific hour; if both BLJ and SLLJ occur, it is defined as a double-LLJ (DLLJ) event.

b. Moisture flux calculation

The boundary layer and low-level moisture flux Q_V at each grid within SC are calculated as follows (Du and Chen 2019a; Li and Du 2021; Montini et al. 2019; Varuolo-Clarke et al. 2022):

$$Q_V = \frac{1}{g}\int_{P_1}^{P_2} qV\,dp, \tag{1}$$

where g is the acceleration of gravity (m s^{-2}), q is the specific humidity (kg kg^{-1}), V denotes the u and v winds (m s^{-1}) at each pressure level, and p is the atmospheric pressure (Pa). Boundary layer and low-level moisture fluxes are vertically integrated from surface to 900 hPa and 900 to 700 hPa, respectively.

The horizontal boundary layer and low-level moisture fluxes Q_T through the south, north, west, and east boundaries of SC during various LLJ events are calculated by integrating Q_V along each boundary of SC:

$$Q_T = \int_{l_1}^{l_2} Q_V\,dl, \tag{2}$$

where the difference between l_1 and l_2 is the length of the south, north, west, and east boundaries of SC, which is indicated by the red rectangle in Figs. 1b, 7, and 8. The net meridional (zonal) moisture flux over SC is the moisture flux difference between the south (west) and north (east) boundary of SC.

In addition, the vertical moisture exchange between the boundary layer and low level over SC during various LLJ events is also analyzed to discuss its possible contribution to the early summer rainfall. The vertical moisture fluxes through the 900- and 700-hPa surface, respectively, over SC are integrated as follows:

$$Q_\omega = \int_{x_1}^{x_2}\int_{y_1}^{y_2} q\omega\,dx\,dy, \tag{3}$$

where ω denotes the vertical velocity at 900- and 700-hPa surface and the difference between $x_1(y_1)$ and $x_2(y_2)$ is the horizontal size of SC in zonal (meridional) direction.

Last, the LLJs-associated moisture budget over the investigated region is calculated based on the following equation (Johnson 1992; Yanai et al. 1973):

$$(\overline{c} - \overline{e}) + \frac{\partial \overline{Q'\omega'}}{\partial p} = -\frac{\partial \overline{Q}}{\partial t} - \overline{V}\nabla\overline{Q} - \overline{\omega}\frac{\partial \overline{Q}}{\partial p}, \tag{4}$$

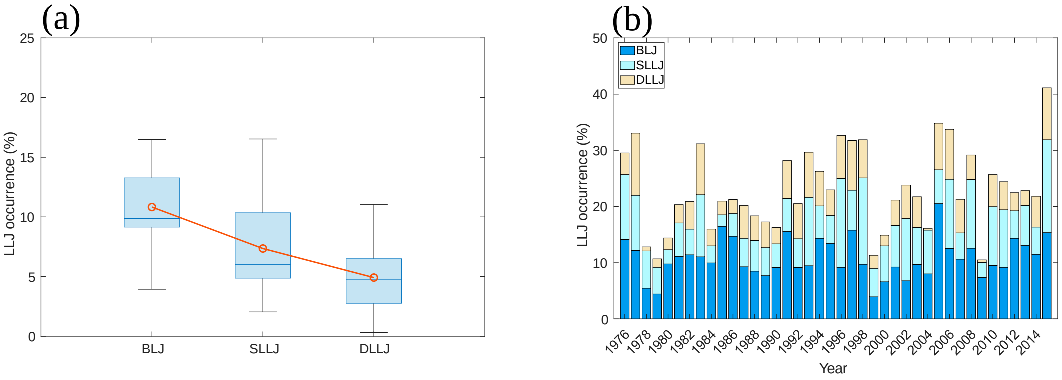

FIG. 2. (a) Annual mean of the occurrence frequency of BLJs, SLLJs, and DLLJs; the red circles represent the mean occurrence frequency of various LLJ events; the lines inside the boxes indicate the medians; the bottom and upper edges of the boxes indicate the lower and upper quartiles; and the lower and upper whiskers represent the minimum and maximum of the occurrence frequencies of various LLJ events; (b) the annual occurrence frequency of BLJ, SLLJ, and DLLJ events over SC during 1976–2015.

where the first term on the right is the moisture tendency and the second and last terms on the right are the horizontal and vertical moisture advection. The sum of the three terms on the left is the subgrid-scale term: *c* and *e* are the precipitation and evaporation rate and the third term on the left is the subgrid-scale transport associated with convection overturning. The overbar indicates a horizontal mean over the grid box and the prime denotes deviations from this mean. The equation measures the apparent moisture sink due to the net condensation and vertical divergence of the vertical eddy transport of energy. The results of the moisture budget calculation are used to diagnose the moisture balance associated with LLJ events.

4. Boundary layer and low-level moisture fluxes during LLJ events

a. *Characteristics of horizontal moisture fluxes for LLJs*

Figure 2 illustrates the occurrence frequency of LLJs in SC during early summer of 1976–2015. Overall, BLJ events exhibit the highest occurrence frequency among all LLJ events, followed by SLLJ and DLLJ events. The mean occurrence frequency of BLJ, SLLJ, and DLLJ events over 1976–2015 is, respectively, 11%, 8%, and 5% of all hours during early summer (Fig. 2a), with significant annual fluctuations (Fig. 2b). The occurrence frequency of SLLJ events demonstrates the most pronounced annual variability, ranging from 2% to 17% of all hours during early summer. On the other hand, the occurrence frequency of BLJ and DLLJ events exhibits a range of 4%–17% and 0%–12% of all hours during early summer, respectively. The interannual variability of the occurrence frequency of LLJs is closely related to the variability of the South China Sea summer monsoon, which is dominated by the variability of the surrounding atmospheric circulations, especially the two subtropical highs over Pacific region, i.e., the western North Pacific subtropical high and the Australian high (Wang et al. 2020). In addition, the interannual variability of the BLJs is also related to the variability of the boundary layer thermal conditions, including the sea surface temperature over the northern South China Sea and the land–sea thermal contrast over South China (Du et al. 2015; Kong et al. 2020). In aggregate, LLJ events occur in 10%–40% of all hours during early summer in SC.

The mean boundary layer and low-level moisture fluxes during various LLJ events are presented and compared with the climatological mean during early summer in Fig. 3. In terms of the climatological mean, both the boundary layer (Fig. 3a) and low-level (Fig. 3b) moisture fluxes exhibit spatial variations that are consistent with spatial patterns of winds at their corresponding layer. The boundary layer moisture flux over land, particularly near mountainous terrain, is substantially lower than that over sea. This is jointly contributed by two reasons. One is the weakening of the boundary layer winds due to larger surface friction over land and the blocking effect of the mountainous terrain. The other is the smaller depth of the vertical moisture flux integration over land, particularly at topography. As illustrated in Fig. 4a, the meridionally average surface pressure of the mountainous terrain at ~25°N can reach nearly 950 hPa, indicating a reduced depth of the boundary layer in this region. For similar reasons, the boundary layer moisture flux splits into two branches at Hainan and reveals two centers to the west and east of Hainan, respectively. The lower boundary layer moisture flux at Hainan corresponds to the highest mountain, Wuzhi Mountain in Hainan. By contrast, the center of the mean low-level moisture flux is situated to the west of SC, corresponding to the location of the maximum wind speed (Fig. 3b), which is further inland compared with the maximum of the boundary layer winds. In the boundary layer, the maximum moisture flux is approximately 150 kg m^{-2} s^{-1}, while the low-level moisture flux reaches approximately 200 kg m^{-2} s^{-1}.

For BLJ events, the maximum boundary layer wind speed is also observed over the sea to the west and east of Hainan, but with a significantly higher wind speed of approximately 10 m s^{-1} compared to the early summer mean. The enhanced winds to the west and east of Hainan results in a substantially

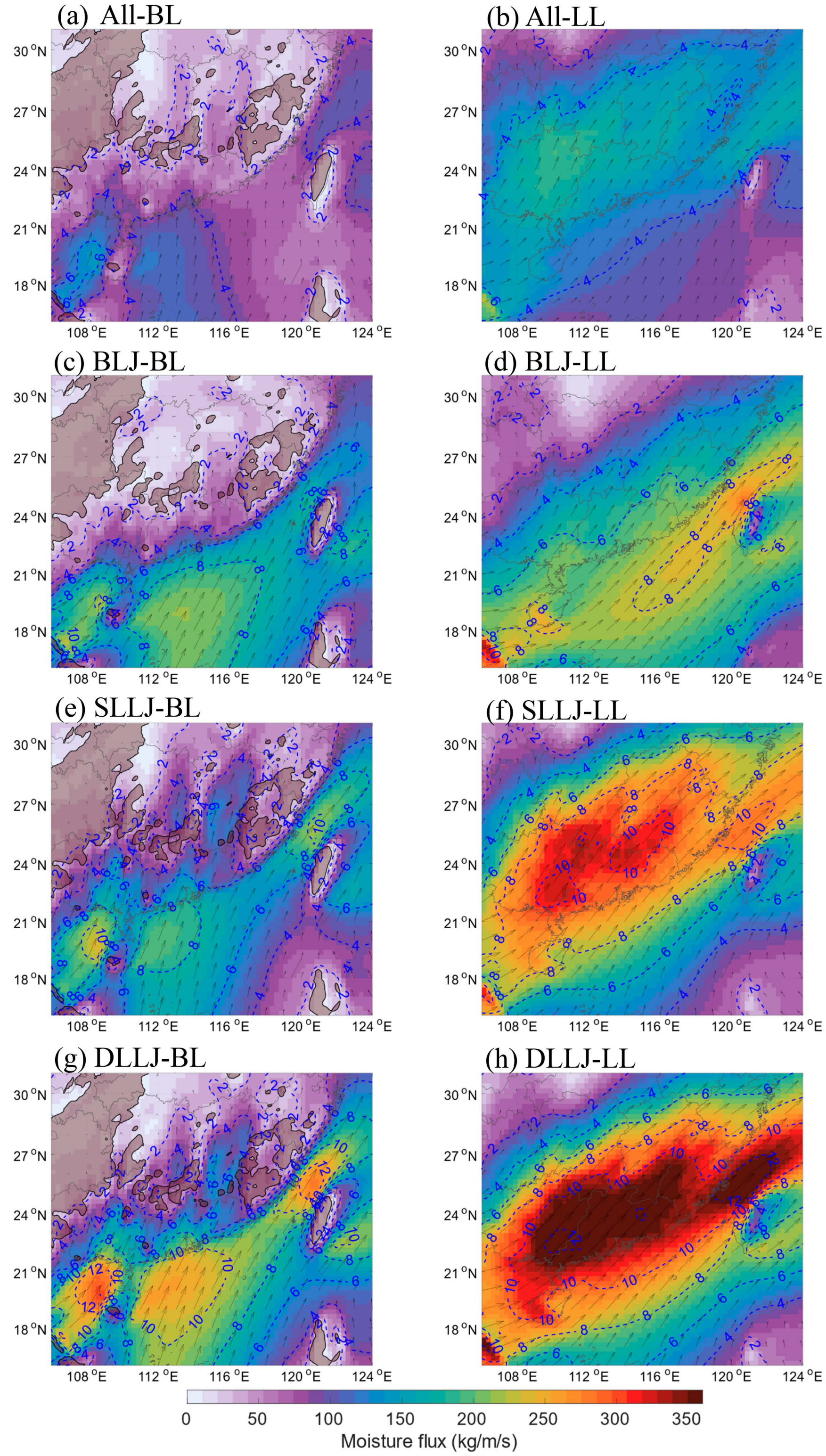

FIG. 3. Mean (left) BL and (right) LL moisture flux (shadings) and horizontal wind field (vectors and contours) for (a),(b) all, (c),(d) BLJ, (e),(f) SLLJ, and (g),(h) DLLJ events during early summer. (left) The shadow indicates topography higher than 500 m.

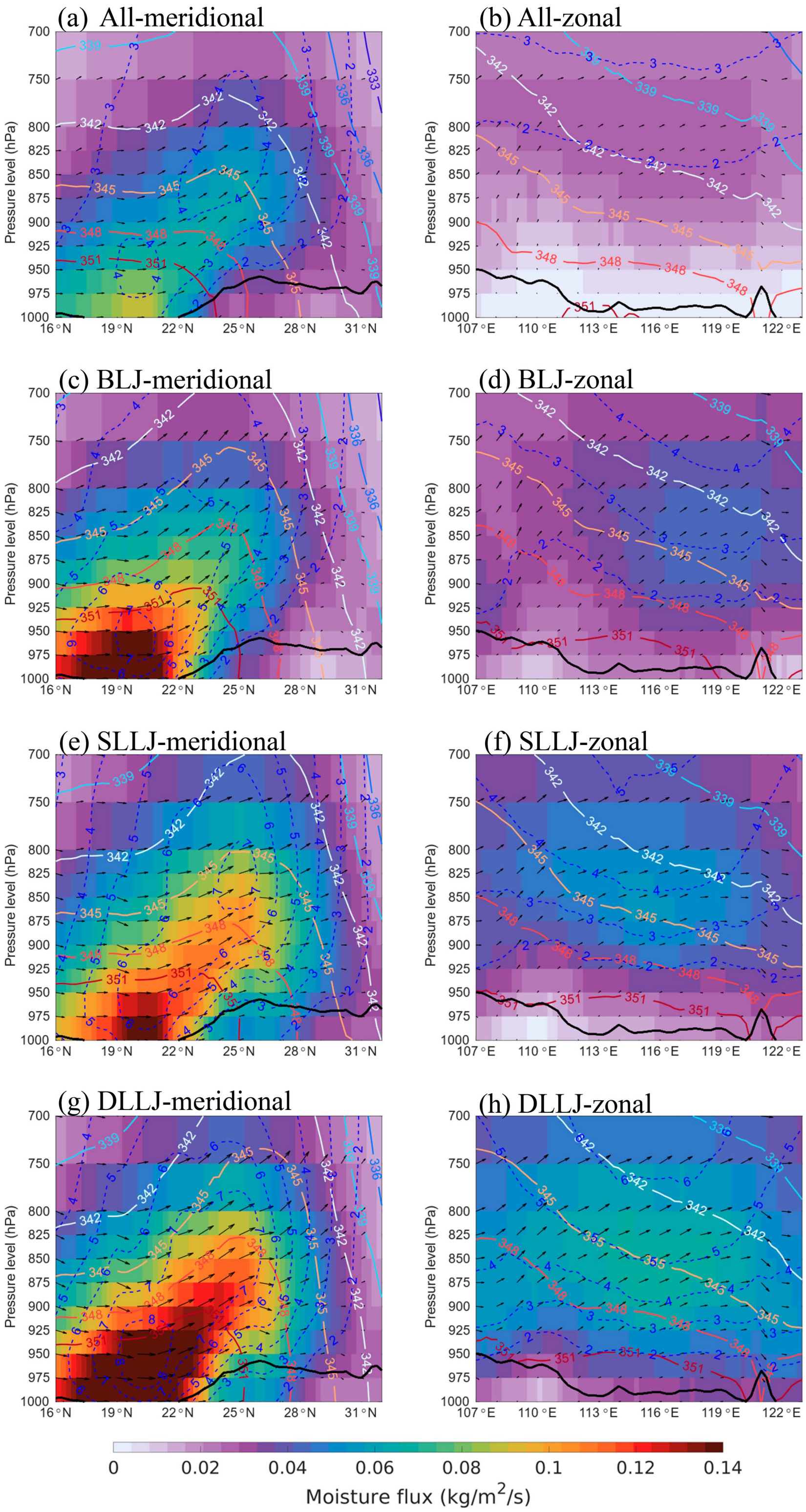

FIG. 4. Cross sections for the mean (left) meridional and (right) zonal moisture flux (shadings) and winds (arrows and contours) for (a),(b) all, (c),(d) BLJ, (e),(f) SLLJ, and (g),(h) DLLJ events during early summer. The mean meridional/zonal profiles are generated by averaging the variables over all longitudes/latitudes in the investigated region shown in Fig. 1. Arrows indicate wind vectors in the (left) y–z plane or (right) x–z plane. The dashed contours indicate velocity of the (left) meridional or (right) zonal wind component, note that the vertical velocity is multiplied by a factor of 50. The solid contours indicate the mean (left) meridional or (right) zonal equivalent potential temperature. The black solid line indicates the mean surface pressure in (left) meridional or (right) zonal direction.

stronger boundary layer moisture flux, reaching a maximum of approximately 250 kg m^{-2} s^{-1} over the sea off the coast of SC (Fig. 3c). Notably, the gradient of wind speed along the coast of SC is significantly enhanced for BLJ events, compared with the climatological mean in Fig. 3a. This augmented gradient of wind speed, which is due to the low-level vortex in the west of SC (Fig. 5c), results in strengthened convergence along the coast, leading to boundary layer moisture convergence at the region. Similarly, the low-level wind speed during BLJ events is generally higher than the climatological mean, with the high values located along the coast of SC at the southeastward side of the vortex (Fig. 5d). The maximum low-level wind speed (~8 m s^{-1}) is located at the Taiwan Strait (Fig. 1a), leading to a maximum moisture flux of approximately 280 kg m^{-2} s^{-1} in that area (Fig. 3d). This maximum moisture flux is induced by a typical barrier jet that usually occurs at the Taiwan Strait during early summer due to the interaction between synoptic systems and coastal orography (Chen et al. 2022).

Regarding SLLJ events, the spatial pattern of the mean boundary layer winds show two differences from the case for BLJ events, as presented in Fig. 3e. One difference is that the wind speed to the west of Hainan is higher, while it is lower to the east during SLLJ events. The two branches of BLJs to the west and the east of Hainan appear frequently during early summer, but with different formation mechanisms. The western branch is jointly contributed by the hydraulic jump jet off the northeast coast of Vietnam, the inertial oscillation effect, as well as the topography in Hainan, while the eastern branch is mainly caused by the diurnal inertial oscillation (Du and Chen 2019a; Kong et al. 2020). As a result, the intensity of the western branch is typically higher than that of the eastern branch. The other difference is that, without evident synoptic systems dominating SC (Fig. 5e), the southwesterly boundary layer winds with a velocity higher than 4 m s^{-1} intrude northward into further inland area during SLLJ events. Consequently, compared to BLJ events, the center of the mean boundary layer moisture flux during SLLJ events is situated over the sea to the west of Hainan, with a maximum value of approximately 280 kg m^{-2} s^{-1}; moreover, the enhanced boundary layer moisture flux exhibits a northward intrusion further inland during SLLJ events, with the front edge reaching ~24°N in the west of SC and ~28°N in the east. The core of the low-level winds for SLLJ events presented in Fig. 3f extends from the Beibu Gulf (Fig. 1a) in the southwest SC to EC, with a maximum wind speed of approximately 10 m s^{-1} (Figs. 3f and 5f). This leads to a substantially higher low-level moisture flux of approximately 350 kg m^{-2} s^{-1} in that area, compared to the case for BLJ events.

The spatial patterns of the mean boundary layer (Fig. 3g) and low-level (Fig. 3h) winds and moisture fluxes for DLLJ events are similar to those of SLLJ events, but with substantially higher values. Notably, the boundary layer moisture flux for DLLJs also shows a northward intrusion to ~28°N (Fig. 3g), which is attributed to the northward intrusion of boundary layer southwesterlies into inland area due to the absence of synoptic system over SC (Fig. 5g). The maximum boundary layer and low-level wind speeds during DLLJ events exceed 12 m s^{-1}, resulting in maximum moisture fluxes of approximately 300 kg m^{-2} s^{-1} in the boundary layer (Fig. 3g) and 400 kg m^{-2} s^{-1} in the low level (Fig. 3h), respectively.

b. *Vertical profiles of the moisture fluxes for LLJs*

The profiles of the mean meridional and zonal moisture fluxes and winds for various LLJ events during early summer are presented and compared with the early summer mean in Fig. 4. As shown in Fig. 4a, the mean meridional moisture flux over SC during early summer exhibit higher values below 950 hPa, particularly to the south of 22°N. This is due to the high moisture concentration in the lower layers of the atmosphere; the meridional moisture flux shows the maximum located off the coast of SC (~20°N), corresponding to the location of the maximum meridional winds. In addition, it shows an upward motion at the southward side of the mountainous terrain at ~25°N, resulting in vertical transport of warm and moist air at the location. This leads to an upward warm and moist tongue stretching to 750 hPa and enhanced northward moisture flux above the boundary layer near 25°N. The mean zonal moisture flux displays a center that stretches from 107° to 120°E within the layer between 850 and 750 hPa, aligning with the location of the maximum zonal winds (Fig. 4b).

During BLJ events, the center of the meridional moisture flux within the boundary layer is at the same location to the early summer mean, but with substantially higher values (Fig. 4c). Compared to the early summer mean, the meridional profile of BLJ events displays a more pronounced upward motion from the coast at 22°N to the mountainous terrain near 25°N, in the layer from surface to 800 hPa (Fig. 4c). This enhanced upward motion is induced by the stronger boundary layer convergence jointly resulted from the land–sea frictional contrast (Bai et al. 2021; Du et al. 2020b; Li et al. 2021; Su et al. 2023; Zhang et al. 2022), the vortex in the west of SC (Li et al. 2020; Luo et al. 2020), and the increasing terrain height from the coast of SC to the mountainous region at ~25°N (Chen et al. 2017; Du and Chen 2019a). The enhanced upward transport of the warm and moist air results in an upward tongue of equivalent potential temperature at ~25°N, leading to a warmer and moistened low level in the region compared to the area to its south or north. The zonal moisture flux displays two centers (Fig. 4d). One is situated to the west of 108°E between 950 and 900 hPa, aligning with the location of the maximum boundary layer moisture flux to the west of Hainan (Fig. 3d), and the other is observed at 850 hPa around 118°E, corresponding to the maximum low-level moisture flux near the Taiwan Strait (Fig. 3d).

For SLLJ events, the maximum meridional moisture flux is also found within the boundary layer at ~20°N (Fig. 4e), but with lower values compared to the BLJ case. Nevertheless, the meridional moisture flux for SLLJ events also exhibits a significant upward motion during the northward transport of warm and moist air from the coast to the mountainous terrain at ~25°N. This results in an upward tongue of equivalent potential temperature at ~25°N. Furthermore, the meridional moisture flux for SLLJ events shows another region of upward motion to the north of 28°N in from the boundary layer

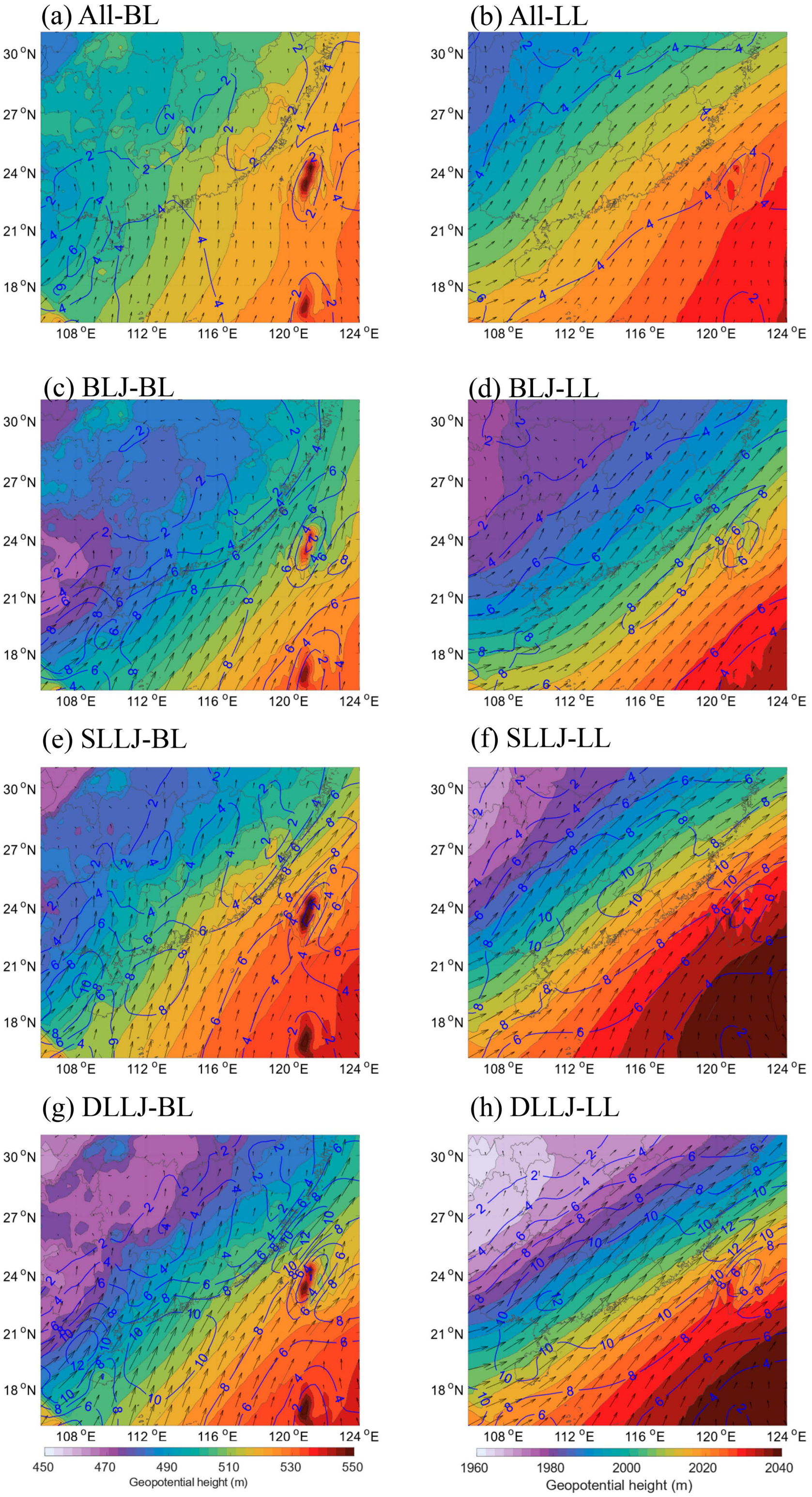

FIG. 5. Mean (left) BL and (right) LL winds (arrows) and geopotential height (shadings) for (a),(b) all, (c),(d) BLJ, (e),(f) SLLJ, and (g),(h) DLLJ events during early summer. The contours indicate the wind speed.

to levels above 850 hPa. This upward motion is likely associated with synoptic systems in the region, such as frontal systems (Chen et al. 2015; Liu et al. 2020; Luo et al. 2020). Compared to BLJ events, the northward transport of boundary layer moisture is enhanced during SLLJ events due to the augmented boundary layer winds over the land area of SC (Fig. 3e). This results in a greater amount of warm and moist air being transported northeastward to the mountainous terrain at ∼25°N, a portion of which is delivered to EC within the boundary layer. The remaining fraction of the warm and moist air is elevated to the SLLJ level by the topography, producing pronounced increase in moisture in the SLLJ level in the region. The enhanced moisture is then transported further downstream by the SLLJ flows. The northeastward-transported moisture in both the boundary layer and the SLLJ level undergoes further elevation along the frontal zone at ∼28°N (Fig. 4e). The maximum zonal moisture flux for SLLJ events is observed at 850 hPa between 110° and 120°E, corresponding to the location of the SLLJ core (Fig. 4f).

The meridional moisture flux for DLLJ events (Fig. 4g) combines the characteristics observed in both BLJ (Fig. 4c) and SLLJ events (Fig. 4e), but with substantially higher values in both the boundary layer and low level. This results in an enhancement in the upward motion during the northeastward transport of the warm and moist air, leading to a deeper tongue of equivalent potential temperature at ∼25°N, and pronounced northeastward moisture transport in both BLJ and SLLJ levels to the frontal zone at ∼28°N. The profile of the zonal moisture flux during DLLJ events is similar with the SLLJ case, but with a lower center located between 900 and 850 hPa and significantly higher values (Fig. 4h).

In general, the mean zonal moisture flux is substantially lower than the meridional moisture flux from the surface to 700 hPa for all LLJ events, indicating that the moisture fluxes over SC are primarily contributed by meridional moisture transport.

c. *Horizontal and vertical moisture fluxes at the boundaries of SC during LLJ events*

The mean horizontal and vertical moisture fluxes at the boundaries of SC during various LLJ events are computed and presented in Fig. 6. Within the boundary layer, the moisture flux shows positive values at the east and south boundaries, as well as the 1000-hPa level, indicating incoming moisture flux in SC. The moisture flux at the south boundary accounts for over 75% of the total incoming moisture flux at the boundaries of SC during BLJ (Fig. 6a), SLLJ (Fig. 6c), and DLLJ (Fig. 6e) events. By contrary, the moisture flux shows negative values at the west and north boundaries and the 900-hPa surface, indicating outgoing moisture flux from SC. The outgoing moisture flux through the 900-hPa surface is the major contributor to the total outgoing moisture flux, indicating upward moisture transport from the boundary layer to higher levels in SC, which is consistent with the results in section 4b.

In the low level, the moisture fluxes at the west and south boundaries and the 900-hPa surface demonstrate comparable contributions to the total incoming moisture flux at the boundaries of SC during various LLJ events (Figs. 6b,d,f). DLLJ events exhibit the largest horizontal incoming moisture fluxes, with the incoming moisture fluxes at the west and south boundaries being ∼6500 and ∼6000 kg m^{-2} s^{-1}, respectively (Fig. 6f). In contrast, BLJ events have the smallest horizontal incoming moisture flux of ∼8600 kg m^{-2} s^{-1} (Fig. 6b). The incoming moisture fluxes at the 900-hPa surface are consistent with the outgoing moisture fluxes in the boundary layer through the 900-hPa surface. The outgoing moisture fluxes at the east boundary of SC for various LLJ events are comparable to each other, with the values ranging from 4000 to 5000 kg m^{-2} s^{-1}. The outgoing moisture fluxes at the north boundary for DLLJ and SLLJ events are ∼9500 kg m^{-2} s^{-1}, significantly higher than that of BLJ events, which is ∼5400 kg m^{-2} s^{-1}. This suggests a close relationship between SLLJ and low-level outgoing moisture flux at the north boundary of SC. Additionally, the outgoing moisture fluxes at the 700-hPa surface for BLJ and DLLJ events (∼3400 and ∼2600 kg m^{-2} s^{-1}) are significantly higher than that for SLLJ events (∼1500 kg m^{-2} s^{-1}), indicating strong upward moisture transport in the low level with the presence of BLJs.

5. Relationship between boundary layer and low-level moisture fluxes of LLJs and regional rainfall patterns

a. *Correlation between moisture fluxes of LLJs and rainfall in SEC*

The correlation between the boundary layer/low-level moisture fluxes over SC during various LLJ events and early summer rainfall at each station over SEC are calculated to investigate the potential linkage between the moisture fluxes of LLJs and early summer rainfall patterns over SEC. It is worth noting that the correlations between early summer rainfall and the difference between the moisture fluxes at the south and north boundaries (net meridional moisture flux) of SC exhibit similar spatial patterns with those between early summer rainfall and the difference between the moisture fluxes at the west and south boundaries (net zonal moisture flux) of SC, albeit with opposite values. This suggests opposite influences of the meridional and zonal moisture fluxes on early summer rainfall over SEC. Furthermore, the correlations for the former are more significant. When considering the mean moisture convergence over SC in calculating the correlations, the relationship becomes less significant, particularly for the boundary layer moisture convergence. This might be due to two factors. First, the variation in meridional and zonal moisture convergence may interfere with each other, reducing the correlation between the mean moisture convergence and early summer rainfall. Second, the boundary layer moisture convergence is significantly influenced by local conditions, such as terrain, land surface properties, and local circulations, making the correlation between moisture convergence and rainfall more complex. To summarize, the correlation analysis suggests a closer relationship between the net meridional moisture fluxes and early summer rainfall over SEC during LLJ events. Consequently, this section focuses solely on

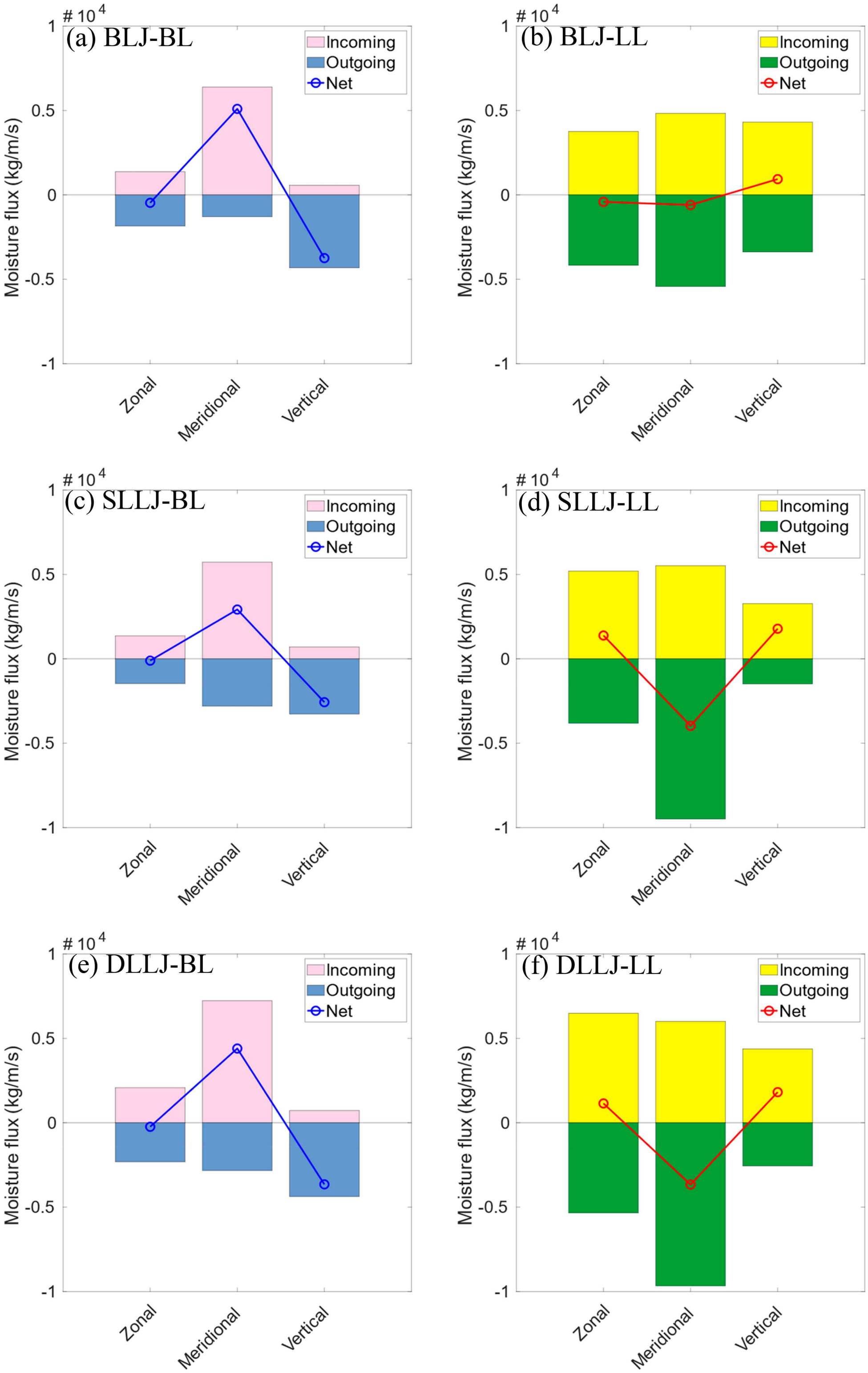

FIG. 6. The mean incoming, outgoing, and net moisture fluxes in the (left) BL and (right) LL over SC for (a),(b) BLJ, (c),(d) SLLJ, and (e),(f) DLLJ events during early summer.

examining and discussing the correlations between early summer rainfall over SEC and the net boundary layer and low-level meridional moisture fluxes over SC.

During BLJ events, a notable positive correlation is observed between the net meridional boundary layer moisture flux over SC and early summer rainfall at stations over the east of SC (Fig. 7a). However, the correlation between net meridional low-level moisture flux and early summer rainfall is less pronounced, despite a significant positive correlation being detected at scattered stations in the east of SC (Fig. 7b). In contrast, no significant correlation is identified between early summer rainfall to the north of SC and both the net meridional boundary layer and low-level moisture fluxes over SC during BLJ events.

Regarding SLLJ events, the net meridional boundary layer moisture flux over SC demonstrates a significant positive correlation with early summer rainfall at stations across the entire SC, except for Hainan, and the south of EC (Fig. 7c). Conversely, the net meridional low-level moisture flux displays a significant negative correlation with early summer rainfall at stations in the north of EC and the northwest of SC, with the most notable correlation occurring between 29° and 31°N (Fig. 7d). The negative correlation can be attributed to the fact that an increase in the net meridional moisture flux over SC enhances the low-level moisture convergence. This promotes the upward transport of low-level moisture over SC, resulting in a lesser amount of low-level moisture being transported to EC, and subsequently leading to reduced rainfall over EC. Additionally, a significant positive correlation is observed between the net meridional low-level moisture flux and early summer rainfall at stations to the south of 21°N.

The correlations between early summer rainfall over SEC and the net meridional boundary layer/low-level moisture fluxes during DLLJ events (Figs. 7e,f) exhibit spatial distributions similar to those observed during SLLJ events. However, there are some differences to note. First, the area with significant positive correlations over SC is smaller compared to the SLLJ case, with the correlation in the southwestern SC becoming insignificant (Fig. 7e). Additionally, the area with significant negative correlations between early summer rainfall and the net meridional low-level moisture flux during DLLJ events are located further southward compared to the SLLJ case, with the most significant correlation found between 27° and 31°N (Fig. 7f).

To summarize, the correlation analysis reveals a significant relationship between early summer rainfall over SEC and the patterns of the net meridional boundary layer and low-level moisture fluxes over SC. These fluxes represent the meridional moisture convergences in the boundary layer and low level over SC, which are influenced by the prevailing type of LLJs in SC. Specifically, a strong net meridional boundary layer moisture flux in SC is associated with enhanced early summer rainfall over the region. Moreover, the presence of SLLJ during SLLJ and DLLJ events appears to amplify the influence of the net meridional boundary layer moisture flux on early summer rainfall in SEC, resulting in a higher correlation over a larger area of SEC. Additionally, in the presence of SLLJ, a weak net meridional low-level moisture flux over SC, indicating a meridional low-level moisture divergence over the region, contributes to enhanced early summer rainfall over EC.

b. *Rainfall patterns associated with net meridional moisture fluxes during LLJs*

To investigate how the configuration of the net meridional boundary layer and low-level moisture fluxes over SC influences the patterns of early summer rainfall over SEC, all LLJ events are collected and categorized into four distinct quadrants based on the intensity levels of the net meridional boundary layer and low-level moisture fluxes. The categorization, as outlined in Table 1, involves assigning events to quadrant 1 (Q1) when both the net meridional boundary layer and low-level moisture fluxes exceed their respective annual means. Quadrant 2 (Q2) encompasses events characterized by a net meridional boundary layer moisture flux below its annual mean and a net meridional low-level moisture flux surpassing its annual mean. Quadrant 3 (Q3) includes events with both the net meridional boundary layer and low-level moisture fluxes falling below their annual means. Finally, quadrant 4 (Q4) comprises events exhibiting a net meridional boundary layer moisture flux exceeding its annual mean and a net meridional low-level moisture flux lower than its annual mean. The composites of hourly rain rate corresponding to each quadrant are presented in Fig. 8.

The mean rainfall of each quadrant exhibits distinct characteristics. In Q1 (Fig. 8a), augmented early summer rainfall is predominantly concentrated over SC, where the mean hourly rain rate exceeds 1 mm h^{-1}. For Q2 (Fig. 8b), the intensified early summer rainfall remains centered at SC, but it becomes more localized along the coast of SC; a substantial intensification of rainfall is observed in EC compared to Q1. Q3 displays the weakest early summer rainfall among all quadrants (Fig. 8c). The enhanced rainfall of Q3 is shifted northward and westward, with the most intense rainfall occurring to the north of 28°N and to the west of 111°E. Finally, Q4 exhibits the largest area of enhanced early summer rainfall among all quadrants (Fig. 8d). The most intense rainfall of Q4 is concentrated along the coast of SC and forms a southwest–northeast band extending from the western SC to EC.

c. *Horizontal and vertical moisture fluxes for various quadrants*

The composites of the boundary layer and low-level moisture fluxes over SEC corresponding to each quadrant are presented in Fig. 9. For Q1, the southwesterly boundary layer and low-level flows (Figs. 9a,b) along the coast of SC are induced by the low-level vortex over SC (Figs. 10a,b). The low-level vortex enhances the pressure gradient in the region, which promotes the intensity of low-level southwesterlies in the southern part of the vortex, as well as the meridional wind shear and convergence in SC. The core of the boundary layer moisture flux is in a southwest–northeast direction and located over the north of the South China Sea (Fig. 9a). The most intensified southwesterly low-level moisture flux is situated along the coast of SC (Fig. 9b), corresponding to the

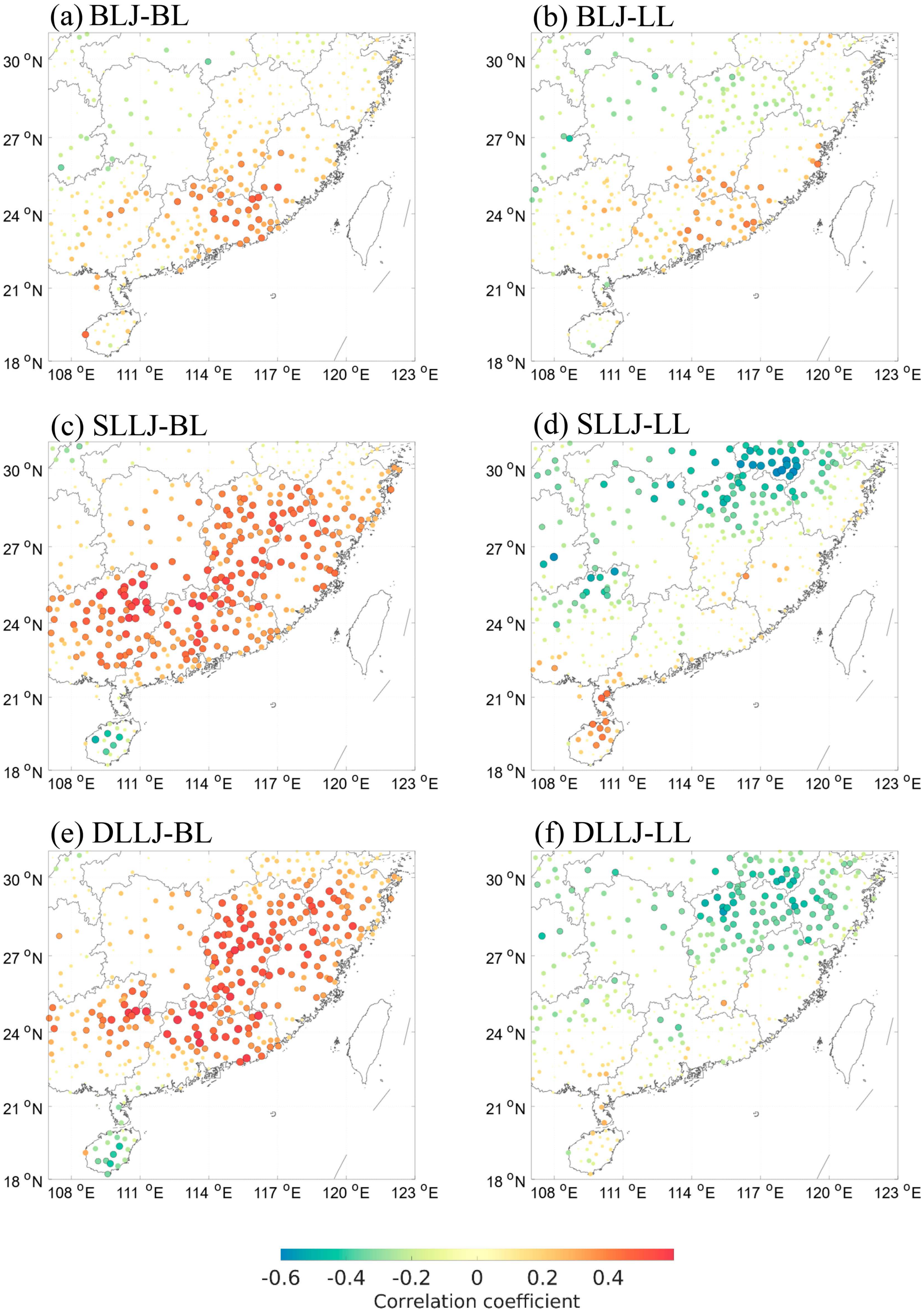

FIG. 7. Correlation coefficient between the early summer rainfall over SEC and the net (left) BL/(right) LL meridional moisture flux over SC for the (a),(b) BLJ, (c),(d) SLLJ, and (e),(f) DLLJ events during early summer.

TABLE 1. Definition of different moisture flux quadrants in terms of the intensities of the net meridional BL and LL moisture fluxes over SC. + indicates net meridional moisture fluxes higher than its respective annual mean; − indicates net meridional moisture fluxes lower than its annual mean.

Net meridional moisture flux (kg m^{-2} s^{-1})	Quadrant			
	Q1	Q2	Q3	Q4
BL	+	−	−	+
LL	+	+	−	−

location of the low-level vortex (Fig. 10b). These patterns of boundary layer and low-level moisture fluxes correspond to southwesterly BLJs and SLLJs at the coast of SC, as indicated by the arrows in Figs. 9a and 9b. This configuration results in strong meridional gradients of wind speed in both the boundary layer and low level over SC and thus the boundary layer and low-level moisture convergence in the region (Figs. 11a,b). As illustrated in Fig. 13a, the most significant gradient of the meridional moisture flux is located near the coast of SC (∼22°N) in the boundary layer, leading to an upward motion from the boundary layer to 700 hPa at the coast. Furthermore, the increasing terrain height from the coast to the mountainous terrain at ∼25°N, combining with the low-level wind shear due to the vortex in the region, results in augmented vertical motion of warm and moist air, leading to an upward tongue of equivalent potential temperature reaching 700 hPa at the topography. These conditions contribute to the development of a strong upward moisture transport mostly confined to SC, producing intense early summer rainfall over SC (Fig. 8a).

Compared with Q1, the mean moisture fluxes for Q2 exhibit lower intensities in both the boundary layer (Fig. 9c) and low level (Fig. 9d), particularly in the boundary layer, under a weak synoptic condition without evident synoptic system dominating SC (Figs. 10c,d). These moisture flux patterns correspond to either weak BLJs located in the north of the South China Sea, combined with weak southwesterly SLLJs or low-level flows along the coast of SC, as indicated by the arrows in Figs. 9c and 9d. The relatively low boundary layer moisture

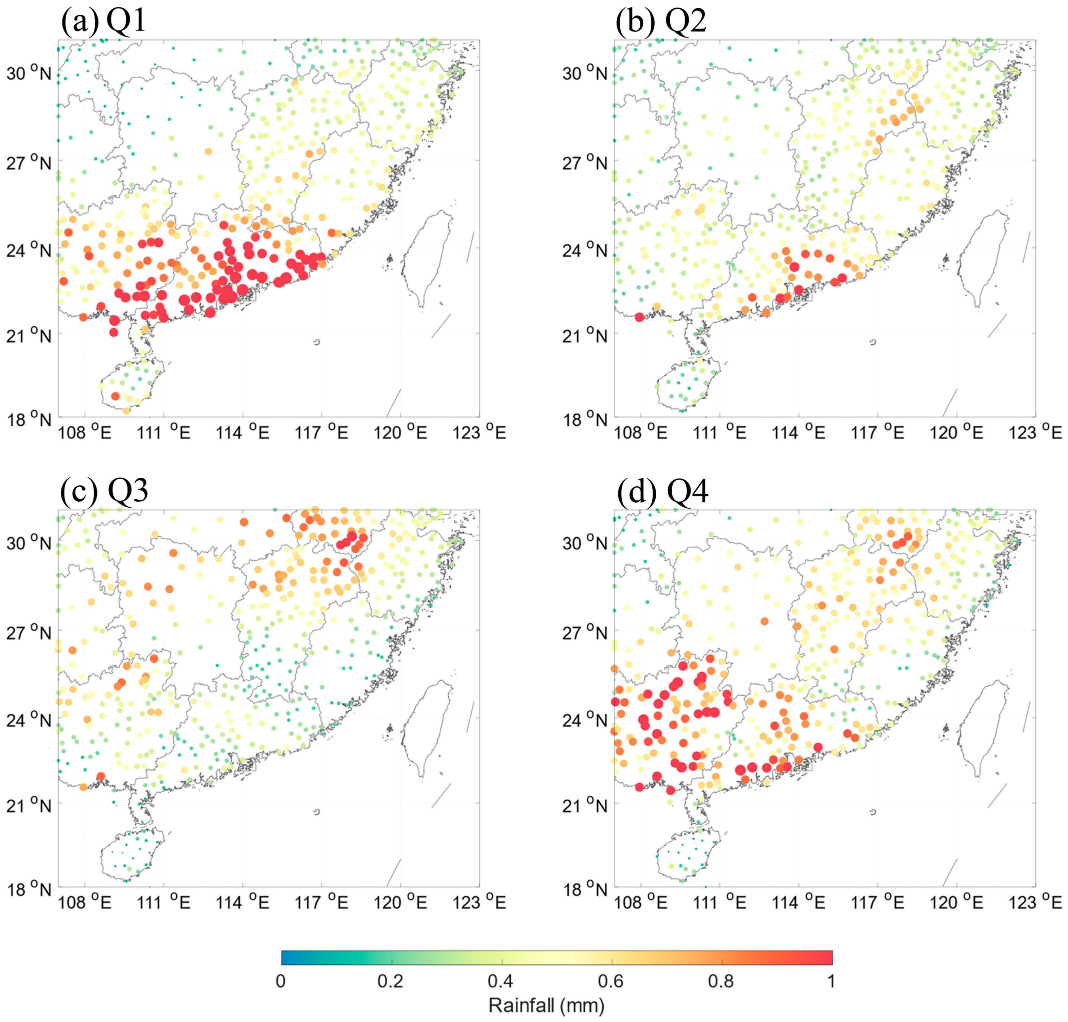

FIG. 8. Mean early summer hourly rain rate over SEC for (a) Q1, (b) Q2, (c) Q3, and (d) Q4.

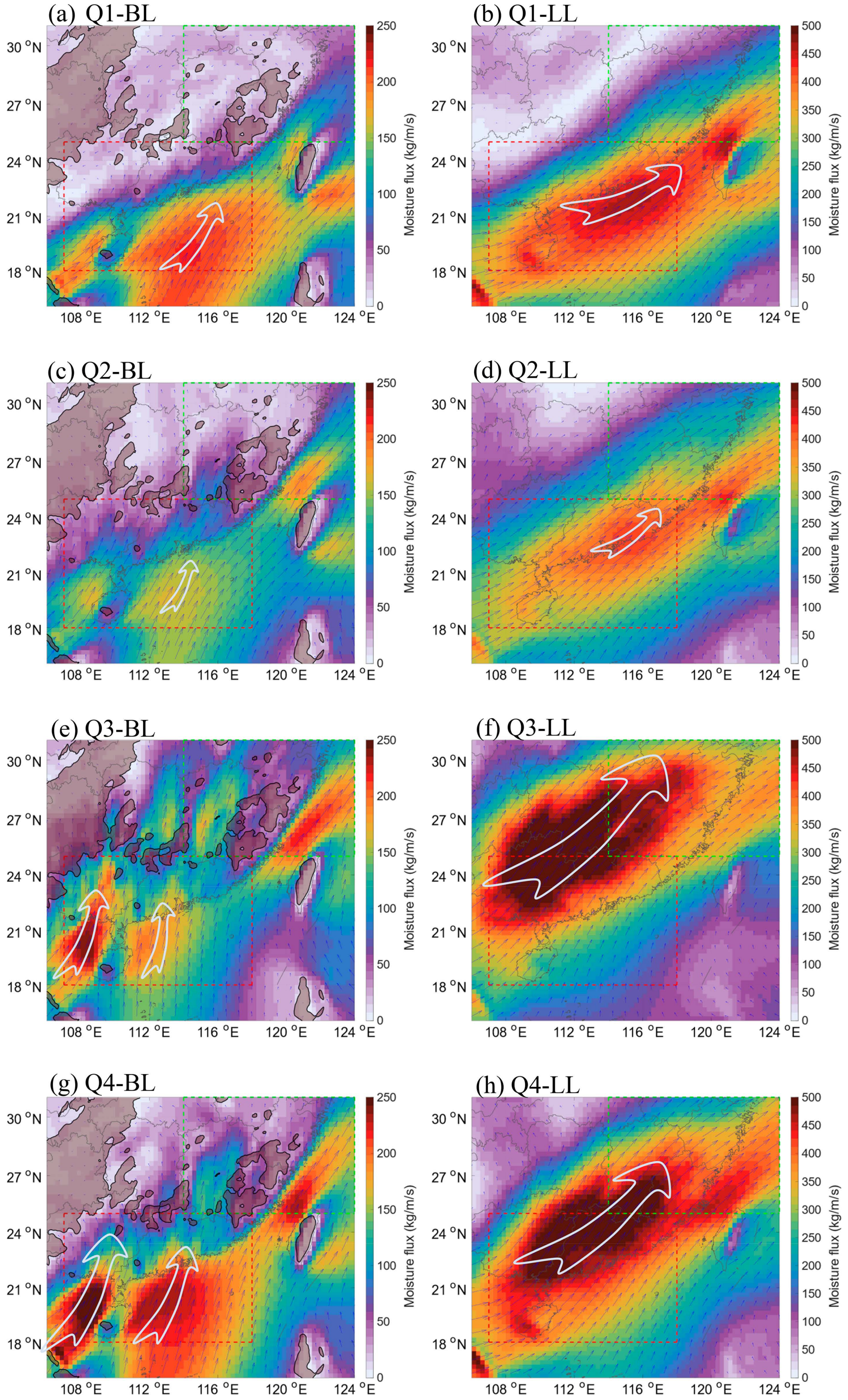

FIG. 9. Mean (left) BL and (right) LL moisture fluxes for (a),(b) Q1, (c),(d) Q2, (e),(f) Q3, and (g),(h) Q4. The red and the green box indicates SC and EC, respectively. The arrows indicate the location and direction of LLJs, and the size of arrows indicates the intensity of LLJs. (left) The shadow indicates topography higher than 500 m.

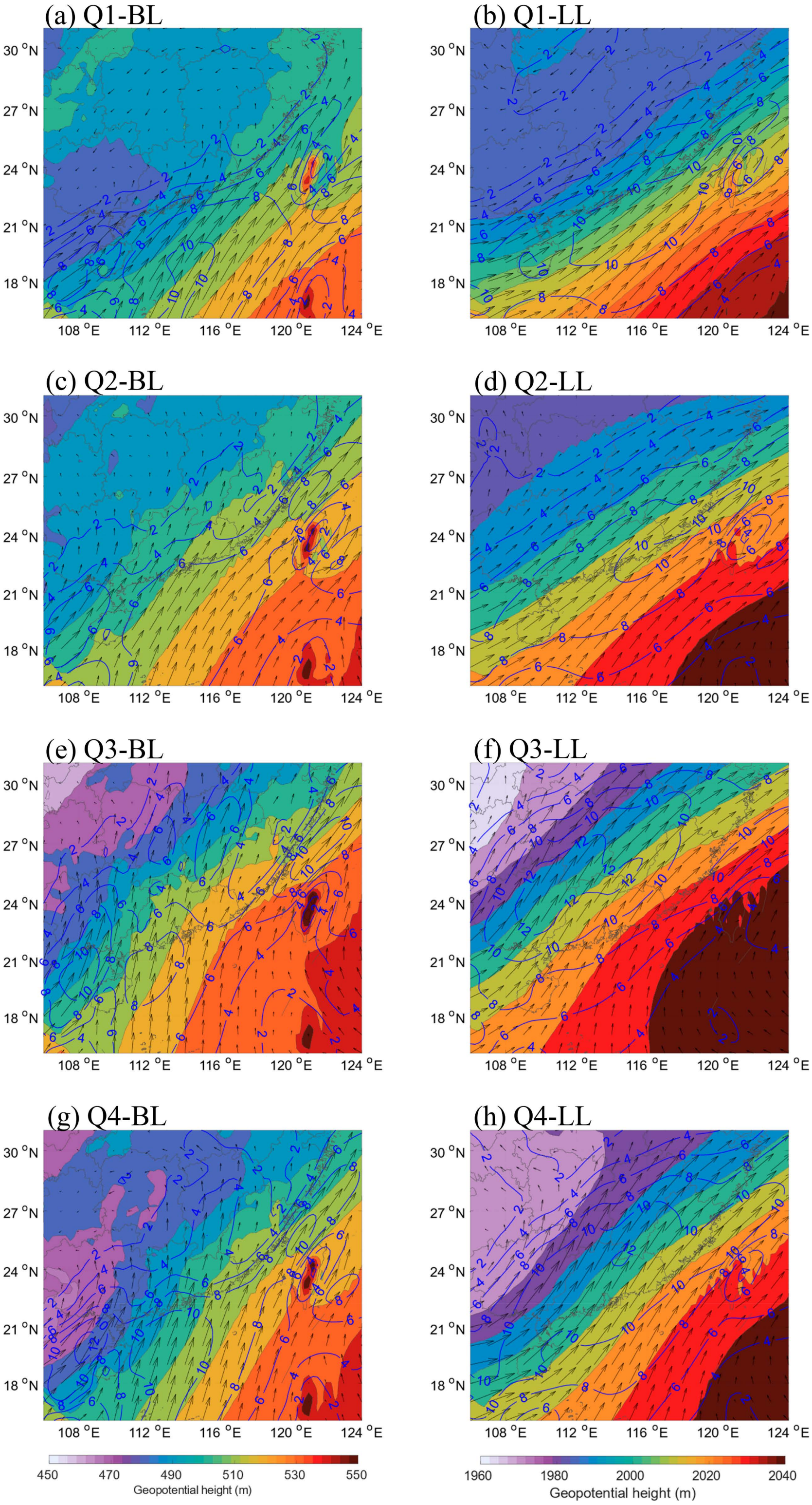

FIG. 10. Mean (left) BL and (right) LL winds (vectors) and geopotential height (shadings) for (a),(b) Q1, (c),(d) Q2, (e),(f) Q3, and (g),(h) Q4. The blue contours indicate horizontal wind speed.

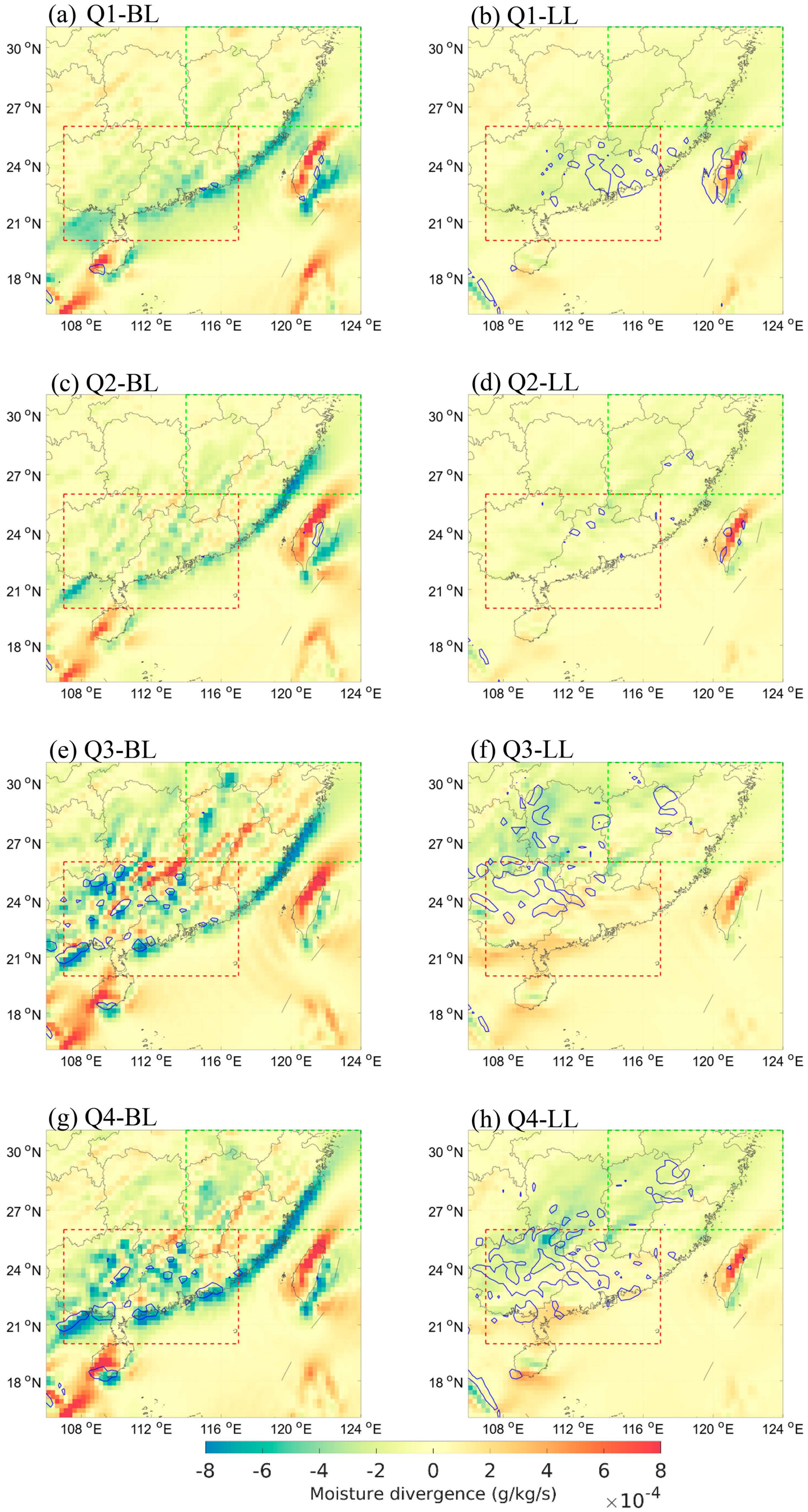

FIG. 11. Mean (left) BL and (right) LL meridional moisture divergence for (a),(b) Q1, (c),(d) Q2, (e),(f) Q3, and (g),(h) Q4. The red and green box indicates SC and EC, respectively. The blue lines indicate vertical velocity greater than 2 cm s^{-1}.

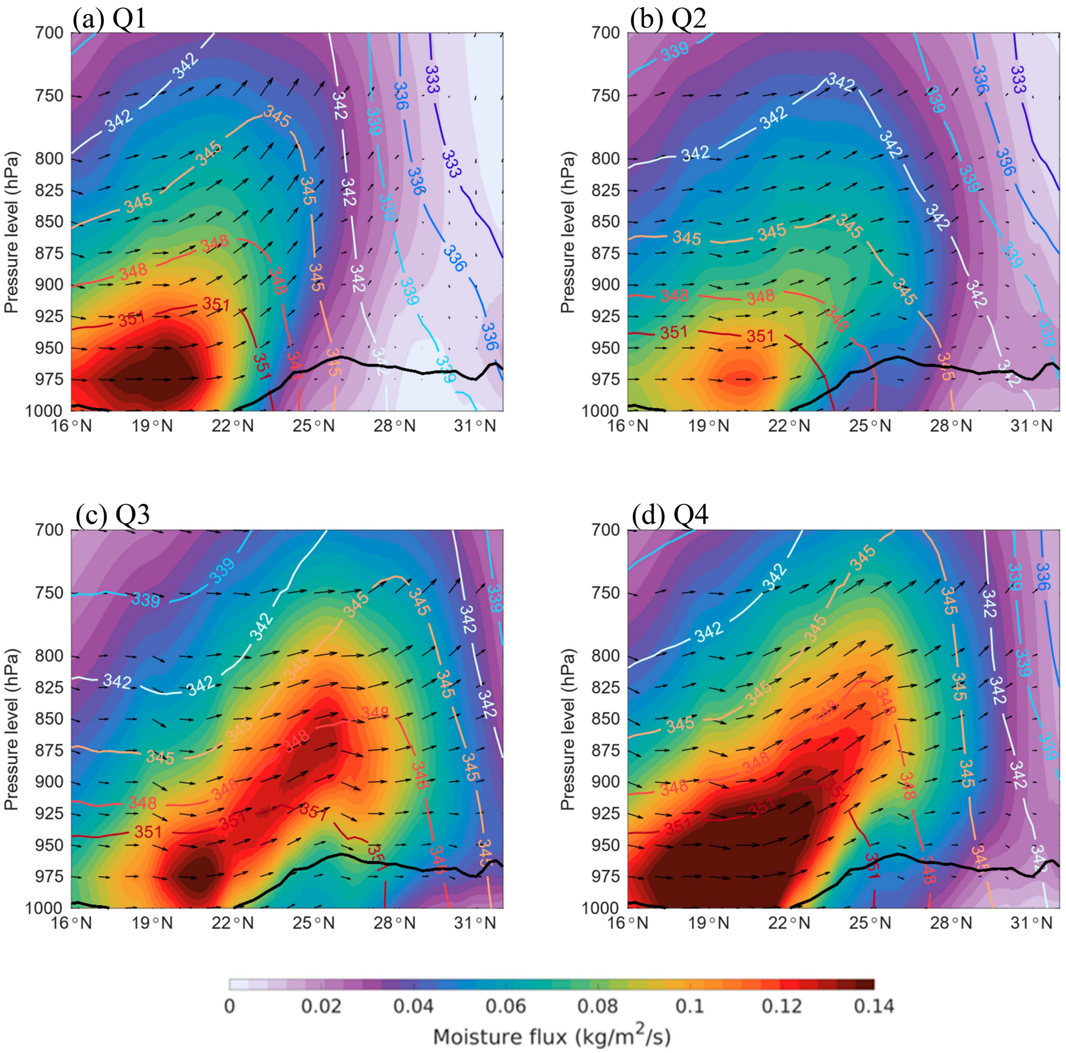

FIG. 12. The cross section for the mean meridional moisture flux (shading colors), meridional wind (vectors), and equivalent potential temperature (contours) for (a) Q1, (b) Q2, (c) Q3, and (d) Q4. The black solid line indicates the mean surface pressure in the meridional direction.

flux (Fig. 9c) results in a considerably weaker meridional moisture convergence (Fig. 11c) at coastal SC, resulting in significantly weaker rainfall in SC (Fig. 8b) compared to Q1. Nevertheless, in the case of Q2, the warm and moist boundary layer air penetrates further northeastward due to the enhanced boundary layer winds over land area of SC and impinges the topography at ~25°N (Fig. 9c). As illustrated by Figs. 9c and 12b, a portion of the warm, moist air bypasses the topography and is transported further northeastward within the boundary layer; the remaining fraction of the warm and moist air is elevated by the topography into levels as high as 750 hPa, leading to an upward tongue of equivalent potential temperature, which leans further northward in the SLLJ level compared with Q1. This indicates a moisture transport from SC to EC at the SLLJ level. The northeastward-transported moisture in both the boundary layer and the SLLJ level is further elevated along the frontal zone at ~28°N (Figs. 10c and 12b), producing rainfall in EC (Fig. 8b). However, the rainfall in EC is weaker than that in SC, due to the generally low intensity of northeastward transport of moisture from SC to EC.

Different from Q1 and Q2, both the boundary layer and low-level moisture flux for Q3 have a quasi-meridional direction (Figs. 9e,f), due to the northward enhancement in the South China Sea summer monsoon (Figs. 10e,f). The southerly boundary layer moisture flux exhibits its maximum intensity over the sea to the west of Hainan (Fig. 9e), leading to moisture convergence at the west of coastal SC (Fig. 11e). The low-level moisture flux shows the highest values across the boundary between SC and EC in a southwest–northeast direction (Fig. 9f), producing a meridional moisture divergence in low level over SC (Fig. 11f). These patterns of boundary layer and low-level moisture fluxes correspond to southerly BLJs over the north of the South China Sea and strong southwesterly SLLJs across the north boundary of SC, as indicated by the arrows in Figs. 9e and 9f. The relatively weak moisture convergence in the boundary layer and divergence in the low level over SC results in significantly less rainfall in SC (Fig. 8c), compared with Q1 and Q2. Nevertheless, Q3 exhibits a pronounced enhancement in the southwesterly boundary layer moisture flux over inland area of SC, resulting in an augmented northeastward penetration of the warm and moist boundary layer air (Fig. 9e). Similar to the case of Q2, a portion of the warm, moist boundary layer air splits into two branches to the west and east of the topography at ~25°N, bypasses the topography, and is transported further northeastward within the boundary layer (Figs. 9e and 12c), resulting in a notable stripe-shaped region of enhanced boundary layer moisture flux extending from coastal SC to EC (Fig. 9e). The remaining fraction of the warm and moist air is elevated above 900 hPa by the topography, leading to an upward warm and moist tongue near the location, and transported further northeastward by the southwesterly SLLJs (Figs. 9f and 12c). The northeastward-transported warm and moist air at both SLLJ and BLJ levels impinges the tilted frontal zone at ~28°N and keeps ascending to higher levels along the front zone, producing enhanced rainfall in EC (Fig. 8c). The roles of topography and secondary circulation associated with front systems in the northward and upward transport of boundary layer moisture from coastal SC to EC are consistent with those described in previous studies (Chen et al. 2022; Du and Chen 2019a; Tu et al. 2019, 2020).

The mean boundary layer moisture flux for Q4 shows a similar pattern to that for Q3 but has the highest intensity among all quadrants. The low-level vortex to the west of SC (Fig. 9g) promotes the gradient of boundary layer moisture flux off the coast of western SC (Fig. 9g) and results in the greatest boundary layer moisture convergence and upward motion at the coast and the topography in the west of SC (Fig. 11g), producing enhanced rainfall in region (Fig. 8d). Figures 9g and 12d further demonstrate that the northeastward-transported boundary layer air also impinges the topography at ~25°N, producing a warm and moist tongue above the boundary layer. After passing the topography, the two branches of the boundary layer moisture flux show a lower intensity than the Q3 case, due to the relatively southwesterly boundary layer winds for Q4 (Figs. 9g and 10g), compared with the southerly winds for Q3 (Figs. 9e and 10e). This leads to a slightly smaller amount of moisture being transported northeastward within the boundary layer (Figs. 9g and 12d). The situation in the SLLJ level for Q4 is similar to Q3. The warm, moist air elevated into the SLLJ level by the topography at ~25°N is transported further downstream by the southwesterly SLLJs, resulting in a low-level moisture divergence over the east of SC (Fig. 11h). The front zone at ~28°N promotes the upward motion of the warm, moist air, generating enhanced rainfall in EC (Fig. 8d). Note that the configuration of Q4 is consistent with the double LLJ event described by Du and Chen (2019a,b), which is closely associated with the occurrence of heavy rainfall in both coastal SC and inland regions.

In summary, the configurations of LLJs plays a crucial role in shaping the spatial pattern of early summer rainfall in SEC. Specifically, the intensity of the meridional boundary layer moisture convergence in SC, which is related with the intensity of BLJs and synoptic conditions in SC, directly influences the intensity of early summer rainfall over SEC. A pronounced meridional boundary layer moisture convergence in SC induced by BLJs leads to intensified rainfall within SC, particularly along the coastal region (Q1 and Q4). On the other hand, enhanced rainfall in EC closely correlates with southwesterly SLLJs over SC (Q3 and Q4), which significantly enhances the northward transport of warm, moist air to EC in addition to the boundary layer moisture transport. In addition, the topography at ~25°N and the tilted front at ~28°N play important roles in the upward transport of moisture and rainfall production in EC. Note that although the correlation between the configuration of LLJs and rainfall pattern does not exhibit a subseasonal transition, the characteristics of LLJs do show subseasonal variations. BLJs and SLLJs confined to coastal SC are closely related with low-level vortex in SC (Q1 and Q2), which primarily occurs in presummer of SC (May–June). By contrary, strong SLLJs located further inland SC (Q3 and Q4) is associated with the northward enhancement of the South China Sea summer monsoon and mei-yu front, which typically occur after mid-June. This subseasonal transition in the characteristics of LLJs leads to a transition in moisture transport pattern and thus rainfall pattern. After mid-June, a larger amount of moisture is transported from SC to regions further northeastward, causing enhanced rainfall in EC.

d. *Moisture budgets in SC and EC*

The moisture budgets in SC (indicated by the red box in Figs. 9 and 11) and EC (indicated by the green box in Figs. 9 and 11) for Q1–4 are presented in Fig. 13 for an in-depth investigation on the moisture dynamics for each quadrant and their contributions to early summer rainfall in SC and EC. Note that the tendency terms for each quadrant in both EC and SC are one order smaller than other terms and thus are negligible.

For SC, the vertical advection term is dominant in the moisture budget from the surface to 700 hPa, particularly for Q1 (Fig. 13a) and Q4 (Fig. 13d). This indicates that early summer rainfall production in SC is mainly caused by vertical motions due to terrain. The integral of the vertical advection term over the boundary layer and low-level is 7.14 and 20.00 g $\mathrm{kg}^{-1}\ \mathrm{s}^{-1}$ for Q1 and 11.5 and 20.46 g $\mathrm{kg}^{-1}\ \mathrm{s}^{-1}$ for Q4 (Tables 2 and 3). It is worth noting that the horizontal advection term shows negative values in a comparable order with the vertical advection term from the surface to 700 hPa, with the minimum located at 900 hPa, particularly for Q3 (Fig. 13c) and Q4 (Fig. 12d). This corresponds to the moisture outgoing from SC through horizontal advection in both the boundary layer and low level for Q3 and Q4 (Figs. 12c,d), with the maximum observed near 900 hPa. This outgoing moisture from SC is mostly attributed to the meridional advection (figure not shown). The integral of the horizontal advection term over the boundary layer and low level

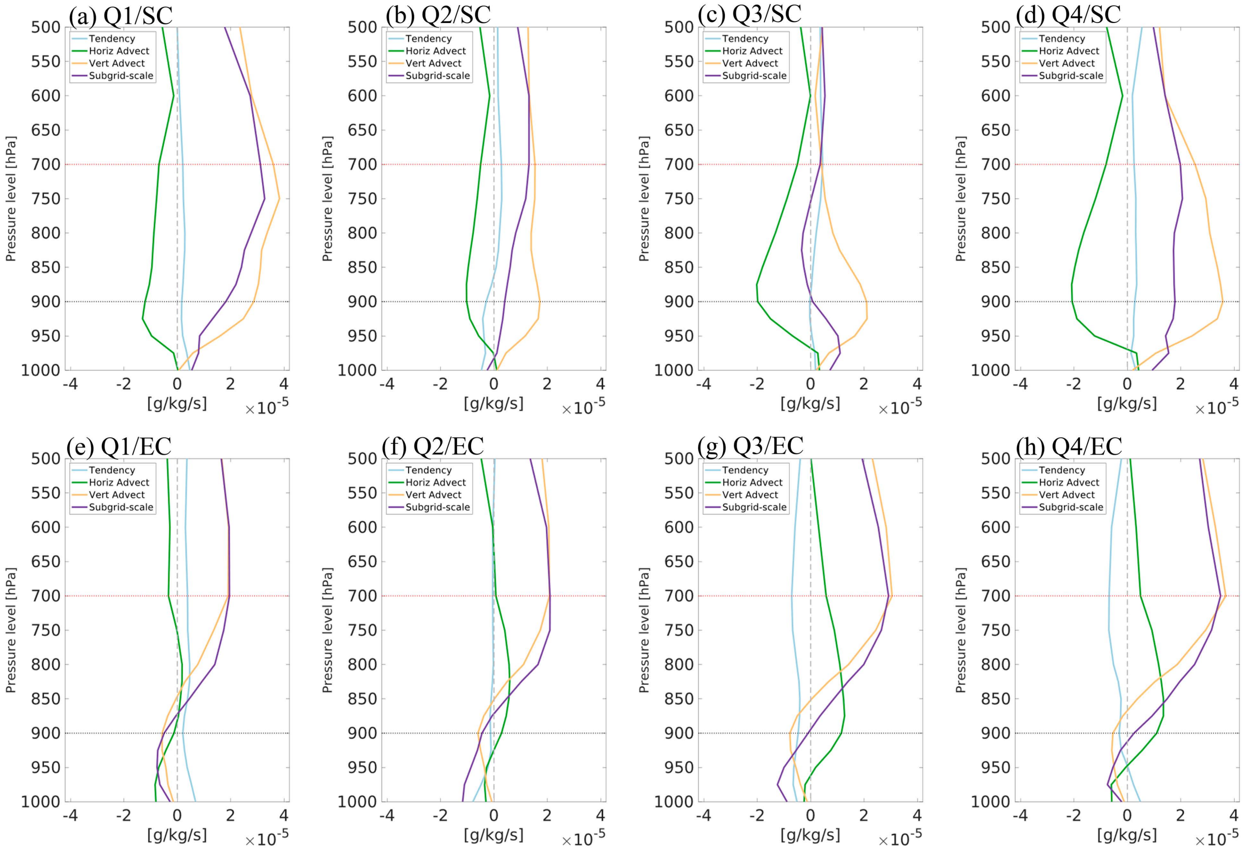

FIG. 13. Vertical profile for the tendency term $(\partial\overline{Q}/\partial t)$, horizontal moisture advection term $(-\overline{V}\nabla\overline{Q})$, vertical moisture advection term $[-\omega(\partial\overline{Q}/\partial p)]$, and subgrid-scale term $[(\overline{c}-\overline{e})+(\partial\overline{Q'\omega'}/\partial p)]$ of the mean apparent moisture sink over (top) SC and (bottom) EC for (a),(e) Q1, (b),(f) Q2, (c),(g) Q3, and (d),(h) Q4.

in SC is −3.11 and −7.63 g kg^{-1} s^{-1} for Q3 and −4.31 and −7.98 g kg^{-1} s^{-1} for Q4, respectively, suggesting a greater amount of moisture outgoing from SC through horizontal advection at the SLLJ level for Q3 and Q4.

For EC, all the terms in the boundary layer show significantly smaller values than those in the low level. Note that the moisture budget below 900 hPa is not reliable for EC due to the mean surface pressure over EC being approximately 950 hPa. In spite of this, the vertical advection term is dominant in the moisture budget above 900 hPa, with the maximum located in 700 hPa for Q3 (Fig. 13g) and Q4 (Fig. 13h), suggesting that rainfall production in EC, particularly above 800 hPa, is mainly contributed by vertical motions due to the frontal system or topography. Nevertheless, the contribution of the horizontal advection term to rainfall production in Q3 and Q4 cannot be omitted. The horizontal advection term reaches the maximum at 900 hPa, with values significantly greater than the vertical advection term below 800 hPa for Q3 and Q4. This indicates a considerable contribution of horizontal moisture advection in the BLJ level and the lower SLLJ level to rainfall production in EC. The integral of horizontal advection term over the low level is 6.22 and 6.55 g kg^{-1} s^{-1} for Q3 and Q4, respectively, and the low-level vertical advection term is 7.1 and 9.7 g kg^{-1} s^{-1} for Q3 and Q4, respectively (Table 3). This horizontal moisture advection is jointly contributed by the meridional and zonal advection due to the

TABLE 2. Terms (10^{-5} g kg^{-1} s^{-1}) for the integrated apparent moisture sink in the BL (1000–900 hPa) average over SC and EC.

Terms	$\partial\overline{Q}/\partial t$		$-\overline{V}\nabla\overline{Q}$		$-\omega(\partial\overline{Q}/\partial p)$		$(\overline{c}-\overline{e})+(\partial\overline{Q'\omega'}/\partial p)$	
Region	SC	EC	SC	EC	SC	EC	SC	EC
Quadrant								
Q1	1.68	2.05	−3.44	−2.89	7.14	−2.07	5.38	−2.92
Q2	−2.32	−1.74	−1.84	0.66	5.78	−1.81	1.62	−4.22
Q3	0.25	−2.82	−3.11	1.63	8.38	−2.59	5.52	−3.78
Q4	1.42	0.20	−4.31	0.40	11.50	−2.12	8.61	−1.52

TABLE 3. Terms (10^{-5} g kg^{-1} s^{-1}) for the integrated apparent moisture sink in the LL (900–700 hPa) averaged over SC and EC.

Terms	$\partial\overline{Q}/\partial t$		$-\overline{V}\nabla\overline{Q}$		$-\omega(\partial\overline{Q}/\partial p)$		$(\overline{c}-\overline{e})+(\partial\overline{Q'\omega'}/\partial p)$	
Region	SC	EC	SC	EC	SC	EC	SC	EC
Quadrant								
Q1	2.27	2.34	−4.78	0.16	20.00	3.90	17.50	6.39
Q2	0.34	−0.43	−3.86	2.64	9.70	5.03	6.18	7.25
Q3	1.48	−3.17	−7.63	6.22	7.07	7.10	0.92	10.15
Q4	2.25	−2.74	−7.98	6.55	20.46	9.70	14.73	13.51

southwesterly SLLJ stretching from SC to EC for Q3 (Figs. 9f and 10f) and Q4 (Figs. 9h and 10h). The low-level moisture budget analysis further demonstrates the contribution of SLLJ level moisture transport from SC to EC to rainfall enhancement in EC described in section 5b and explains the negative correlation between the net meridional low-level moisture flux and early summer rainfall in EC, particularly during SLLJ and DLLJ events (Figs. 7d,f).

6. Conclusions and discussion

Low-level jets (LLJs) play an important role in rainfall through transporting abundant warm and moist air, vital for convection activities. In this study, we delve into the impact of two distinct LLJ types, the synoptic-system-related LLJ (SLLJ) and boundary layer jet (BLJ), on rainfall mechanisms. By utilizing a long-term rain gauge record in China and an atmospheric reanalysis dataset during 1976–2015, we scrutinize different configurations of SLLJ and BLJ, encompassing pure SLLJ, pure BLJ, and double-LLJ (DLLJ) events. Our focus lies in understanding their moisture flux and convergence patterns in South China (SC) and their relationships with the early summer rainfall patterns over South and East China (SEC).

The results reveal a positive net meridional moisture flux in the boundary layer over SC during all LLJ events, particularly during BLJ events. By contrary, negative net meridional moisture flux is observed in the low level over SC when SLLJ occurs during SLLJ and DLLJ events. Furthermore, the net meridional boundary layer/low-level moisture fluxes, which vary with different configurations of LLJs, exhibit a close relationship with the spatial pattern of early summer rainfall in SEC.

The presence of BLJs, observed during BLJ and DLLJ events, leads to robust meridional boundary layer moisture fluxes off the coast of SC. The boundary layer wind convergence due to low-level vortex, land–sea contrast, coastal terrain, and in SC results in strong moisture convergence and upward motions at coastal SC and consequently amplifies rainfall in the region. SLLJs, observed during SLLJ and DLLJ events, enhance the influence of boundary layer moisture fluxes on early summer rainfall over a wider area, leading to a stronger correlation between boundary layer moisture fluxes and the early summer rainfall in SEC. Specifically, southwesterly SLLJs sitting over inland SC indicates an increased meridional low-level moisture flux through the north border of SC. This results in abundant moisture being transported northward to EC in the low level, leading to enhanced early summer rainfall in the region.

Further categorizing LLJ events based on the intensity of the net boundary layer/low-level meridional moisture fluxes over SC unveils the significant roles of LLJs in determining the pattern of early summer rainfall over SEC. The intensity of BLJs directly influences the intensity of early summer rainfall over SEC. On the one hand, strong BLJs promote trigger intense moisture convergence at the coast of SC, uplifting boundary layer moisture to higher altitudes and generating rainfall in the region and downstream areas (Q1 and Q4). Conversely, weak BLJs tend to produce weak rainfall in SEC (Q2 and Q3). On the other hand, the location of rainfall is closely related to the direction/location of LLJs affected by synoptic conditions.

A low-level vortex sitting in the west of SC tends to confine the southwesterly BLJs and SLLJs to coastal SC, which promotes a meridional moisture convergence over SC in the boundary layer and low level. This leads to strong upward moisture transport in SC, producing rainfall mainly in the region (Q1 and Q2), as illustrated in Fig. 14a. By contrary, the absence of evident synoptic systems in SC results in northeastward extension of BLJ flows from the coast to inland SC, leading to northeastward transport of warm and air to further inland area in the boundary layer. A portion of the boundary layer warm and moist air impinges the topography at ~25°N, splits into two branches to the west and east of the topography, bypasses the topography, and is transported further northward within the boundary layer; the remaining fraction is elevated above the boundary layer by the topography, leading to an upward warm and moist tongue above the topography, and transported further northward by southwesterly SLLJs. The northeastward-transported warm and moist air in both the BLJ and SLLJ level impinges the frontal zone at ~28°N and is further elevated to higher levels, producing enhanced rainfall in EC (Q3 and Q4), as illustrated in Fig. 14b. In particular, when a strong BLJ stretching from the coast to inland SC coincides with a strong southwesterly SLLJ situated over inland SC, it promotes moisture convergence in SC, as well as the moisture transport to EC in both BLJ and SLLJ levels, leading to enhanced rainfall in both SC and EC (Q4).

This study sheds a light on the distinct yet equally crucial roles of SLLJs and BLJs in shaping early summer rainfall patterns over SEC in a climatological manner. Our results underscore the need for further investigation to quantitatively understand the individual and interactive influences of SLLJs and BLJs on early summer rainfall across various SEC regions.

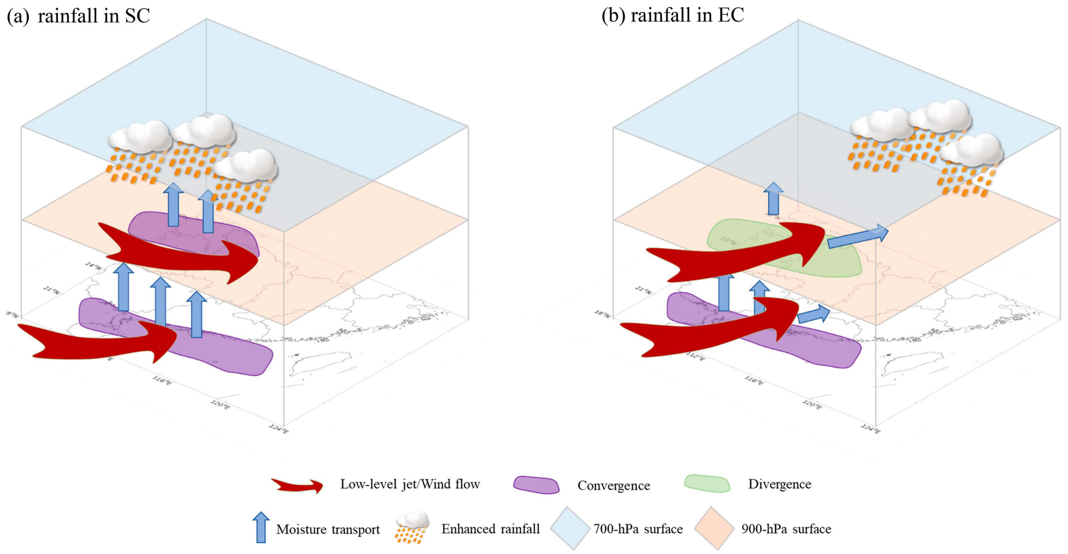

FIG. 14. Schematic illustration for the roles of BL and LLJs in modulating early summer rainfall in SC. (a) Enhanced early summer rainfall in SC and (b) enhanced early summer rainfall in EC.

Acknowledgments. This work was supported by the National Natural Science Foundation of China (Grants U2242203 and 42122033), the Guangdong Basic and Applied Basic Research Foundation (Grants 2022A1515110925 and 2024A1515012571), and the Key Innovation Team of China Meteorological Administration (CMA2023ZD08). The authors are deeply grateful to the editor (Dr. Wenhong Li) and four anonymous reviewers for taking the time to review our work and provide constructive comments and suggestions.

Data availability statement. Stationary rainfall observations over South China provided by the China Meteorological Administration were used in this study (Su 2023).

REFERENCES

Bai, L., G. Chen, Y. Huang, and Z. Meng, 2021: Convection initiation at a coastal rainfall hotspot in South China: Synoptic patterns and orographic effects. *J. Geophys. Res. Atmos.*, **126**, e2021JD034642, https://doi.org/10.1029/2021JD034642.

Beebe, R. G., and F. C. Bates, 1955: A mechanism for assisting in the release of convective instability. *Mon. Wea. Rev.*, **83** (1), 1–10, https://doi.org/10.1175/1520-0493(1955)083<0001:AMFAIT>2.0.CO;2.

Bonner, W. D., 1968: Climatology of the low level jet. *Mon. Wea. Rev.*, **96**, 833–850, https://doi.org/10.1175/1520-0493(1968)096<0833:COTLLJ>2.0.CO;2.

Chao, L., B. Huang, Y. Yuanjian, P. Jones, J. Cheng, Y. Yang, and Q. Li, 2020: A new evaluation of the role of urbanization to warming at various spatial scales: Evidence from the Guangdong-Hong Kong-Macau region, China. *Geophys. Res. Lett.*, **47**, e2020GL089152, https://doi.org/10.1029/2020GL089152.

Chen, G. T.-J., and C.-C. Yu, 1988: Study of low-level jet and extremely heavy rainfall over northern Taiwan in the Mei-Yu season. *Mon. Wea. Rev.*, **116**, 884–891, https://doi.org/10.1175/1520-0493(1988)116<0884:SOLLJA>2.0.CO;2.

Chen, S., R. Cao, Y. Xie, Y. Zhang, W. Tan, H. Chen, P. Guo, and P. Zhao, 2021: Study of the seasonal variation in Aeolus wind product performance over China using ERA5 and radiosonde data. *Atmos. Chem. Phys.*, **21**, 11 489–11 504, https://doi.org/10.5194/acp-21-11489-2021.

Chen, X., F. Zhang, and K. Zhao, 2017: Influence of monsoonal wind speed and moisture content on intensity and diurnal variations of the mei-yu season coastal rainfall over south China. *J. Atmos. Sci.*, **74**, 2835–2856, https://doi.org/10.1175/JAS-D-17-0081.1.

Chen, Y., Y. Li, and T. Zhao, 2015: Cause analysis on eastward movement of Southwest China vortex and its induced heavy rainfall in South China. *Adv. Meteor.*, **2015**, 481735, https://doi.org/10.1155/2015/481735.

Chen, Y.-L., C.-C. Tu, F. Hsiao, C.-S. Chen, P.-L. Lin, and P.-H. Lin, 2022: An overview of low-level jets (LLJs) and their roles in heavy rainfall over the Taiwan area during the early summer rainy season. *Meteorology*, **1**, 64–112, https://doi.org/10.3390/meteorology1010006.

Cui, C., W. Zhou, H. Yang, X. Wang, Y. Deng, X. Wang, G. Xu, and J. Wang, 2023: Analysis of the characteristics of the low-level jets in the middle reaches of the Yangtze River during the mei-yu season. *Adv. Atmos. Sci.*, **40**, 711–724, https://doi.org/10.1007/s00376-022-2107-1.

Du, Y., and G. Chen, 2019a: Climatology of low-level jets and their impact on rainfall over southern China during the early-summer rainy season. *J. Climate*, **32**, 8813–8833, https://doi.org/10.1175/JCLI-D-19-0306.1.

——, and ——, 2019b: Heavy rainfall associated with double low-level jets over southern China. Part II: Convection initiation. *Mon. Wea. Rev.*, **147**, 543–565, https://doi.org/10.1175/MWR-D-18-0102.1.

——, Q. Zhang, Y. Ying, and Y. Yang, 2012: Characteristics of low-level jets in Shanghai during the 2008-2009 warm seasons as inferred from wind profiler radar data. *J. Meteor. Soc. Japan*, **90**, 891–903, https://doi.org/10.2151/jmsj.2012-603.

——, ——, Y. l. Chen, Y. Zhao, and X. Wang, 2014: Numerical simulations of spatial distributions and diurnal variations of low-level jets in China during early summer. *J. Climate*, **27**, 5747–5767, https://doi.org/10.1175/JCLI-D-13-00571.1.

——, Y.-L. Chen, and Q. Zhang, 2015: Numerical simulations of the boundary layer jet off the southeastern coast of China. *Mon. Wea. Rev.*, **143**, 1212–1231, https://doi.org/10.1175/MWR-D-14-00348.1.

——, G. Chen, B. Han, C. Mai, L. Bai, and M. Li, 2020a: Convection initiation and growth at the coast of South China. Part I: Effect of the marine boundary layer jet. *Mon. Wea. Rev.*, **148**, 3847–3869, https://doi.org/10.1175/MWR-D-20-0089.1.

——, ——, ——, L. Bai, and M. Li, 2020b: Convection initiation and growth at the coast of South China. Part II: Effects of the terrain, coastline, and cold pools. *Mon. Wea. Rev.*, **148**, 3871–3892, https://doi.org/10.1175/MWR-D-20-0090.1.

——, Y. Shen, and G. Chen, 2022: Influence of coastal marine boundary layer jets on rainfall in South China. *Adv. Atmos. Sci.*, **39**, 782–801, https://doi.org/10.1007/s00376-021-1195-7.

Guo, J., and Coauthors, 2021: Technical note: First comparison of wind observations from ESA's satellite mission Aeolus and ground-based radar wind profiler network of China. *Atmos. Chem. Phys.*, **21**, 2945–2958, https://doi.org/10.5194/acp-21-2945-2021.

He, Y., K. Wang, and F. Feng, 2021: Improvement of ERA5 over ERA-Interim in simulating surface incident solar radiation throughout China. *J. Climate*, **34**, 3853–3867, https://doi.org/10.1175/JCLI-D-20-0300.1.

Helfand, H. M., and S. D. Schubert, 1995: Climatology of the simulated Great Plains low-level jet and its contribution to the continental moisture budget of the United States. *J. Climate*, **8**, 784–806, https://doi.org/10.1175/1520-0442(1995)008<0784:COTSGP>2.0.CO;2.

Hersbach, H., and Coauthors, 2020: The ERA5 global reanalysis. *Quart. J. Roy. Meteor. Soc.*, **146**, 1999–2049, https://doi.org/10.1002/qj.3803.

Higgins, R. W., Y. Yao, E. S. Yarosh, J. E. Janowiak, and K. C. Mo, 1997: Influence of the Great Plains low-level jet on summertime precipitation and moisture transport over the central United States. *J. Climate*, **10**, 481–507, https://doi.org/10.1175/1520-0442(1997)010<0481:IOTGPL>2.0.CO;2.

Huang, X., C. Zhang, J. Fei, X. Cheng, J. Ding, and H. Liu, 2022: Uplift mechanism of coastal extremely persistent heavy rainfall (EPHR): The key role of low-level jets and ageostrophic winds in the boundary layer. *Geophys. Res. Lett.*, **49**, e2021GL096029, https://doi.org/10.1029/2021GL096029.

Jiang, Q., and Coauthors, 2021: Evaluation of the ERA5 reanalysis precipitation dataset over Chinese Mainland. *J. Hydrol.*, **595**, 125660, https://doi.org/10.1016/j.jhydrol.2020.125660.

Jiang, Y., S. Han, C. Shi, T. Gao, H. Zhen, and X. Liu, 2021: Evaluation of HRCLDAS and ERA5 datasets for near-surface wind over Hainan Island and South China Sea. *Atmosphere*, **12**, 766, https://doi.org/10.3390/atmos12060766.

Jiao, D., N. Xu, F. Yang, and K. Xu, 2021: Evaluation of spatial-temporal variation performance of ERA5 precipitation data in China. *Sci. Rep.*, **11**, 17956, https://doi.org/10.1038/s41598-021-97432-y.

Johnson, R. H., 1992: Heat and moisture sources and sinks of Asian monsoon precipitating systems. *J. Meteor. Soc. Japan*, **70**, 353–372, https://doi.org/10.2151/jmsj1965.70.1B_353.

King, J. A., S. Engelstaedter, R. Washington, and C. Munday, 2021: Variability of the Turkana low-level jet in reanalysis and models: Implications for rainfall. *J. Geophys. Res. Atmos.*, **126**, e2020JD034154, https://doi.org/10.1029/2020JD034154.

Kong, H., Q. Zhang, Y. Du, and F. Zhang, 2020: Characteristics of coastal low-level jets over Beibu Gulf, China, during the early warm season. *J. Geophys. Res. Atmos.*, **125**, e2019JD031918, https://doi.org/10.1029/2019JD031918.

Li, H., Y. Huang, S. Hu, N. Wu, X. Liu, and H. Xiao, 2021: Roles of terrain, surface roughness, and cold pool outflows in an extreme rainfall event over the coastal region of South China. *J. Geophys. Res. Atmos.*, **126**, e2021JD035556, https://doi.org/10.1029/2021JD035556.

Li, X., and Y. Du, 2021: Statistical relationships between two types of heavy rainfall and low-level jets in South China. *J. Climate*, **34**, 8549–8566, https://doi.org/10.1175/JCLI-D-21-0121.1.

Li, Z., Y. Luo, Y. Du, and J. C. L. Chan, 2020: Statistical characteristics of pre-summer rainfall over South China and associated synoptic conditions. *J. Meteor. Soc. Japan*, **98**, 213–233, https://doi.org/10.2151/jmsj.2020-012.

Liu, H., M. He, B. Wang, and Q. Zhang, 2014: Advances in low-level jet research and future prospects. *J. Meteor. Res.*, **28**, 57–75, https://doi.org/10.1007/s13351-014-3166-8.

Liu, L., H. Gu, J. Xie, and Y. P. Xu, 2021: How well do the ERA-Interim, ERA-5, GLDAS-2.1 and NCEP-R2 reanalysis datasets represent daily air temperature over the Tibetan Plateau? *Int. J. Climatol.*, **41**, 1484–1505, https://doi.org/10.1002/joc.6867.

Liu, X., Y. Luo, L. Huang, D. L. Zhang, and Z. Guan, 2020: Roles of double low-level jets in the generation of coexisting inland and coastal heavy rainfall over south China during the presummer rainy season. *J. Geophys. Res. Atmos.*, **125**, e2020JD032890, https://doi.org/10.1029/2020JD032890.

Luo, Y., 2017: Advances in understanding the early-summer heavy rainfall over South China. *The Global Monsoon System: Research and Forecast*, World Scientific, 215–226.

——, R. Xia, and J. C. L. Chan, 2020: Characteristics, physical mechanisms, and prediction of pre-summer rainfall over South China: Research progress during 2008–2019. *J. Meteor. Soc. Japan*, **98**, 19–42, https://doi.org/10.2151/jmsj.2020-002.

Marengo, J. A., M. W. Douglas, and P. L. Silva Dias, 2002: The South American low-level jet east of the Andes during the 1999 LBA-TRMM and LBA-WET AMC campaign. *J. Geophys. Res.*, **107**, 8079, https://doi.org/10.1029/2001JD001188.

Monaghan, A. J., D. L. Rife, J. O. Pinto, C. A. Davis, and J. R. Hannan, 2010: Global precipitation extremes associated with diurnally varying low-level jets. *J. Climate*, **23**, 5065–5084, https://doi.org/10.1175/2010JCLI3515.1.

Montini, T. L., C. Jones, and L. M. V. Carvalho, 2019: The South American low-level jet: A new climatology, variability, and changes. *J. Geophys. Res. Atmos.*, **124**, 1200–1218, https://doi.org/10.1029/2018JD029634.

Munday, C., R. Washington, and N. Hart, 2021: African low-level jets and their importance for water vapor transport and rainfall. *Geophys. Res. Lett.*, **48**, e2020GL090999, https://doi.org/10.1029/2020GL090999.

Song, Y., and J. Wei, 2021: Diurnal cycle of summer precipitation over the North China Plain and associated land–atmosphere interactions: Evaluation of ERA5 and MERRA-2. *Int. J. Climatol.*, **41**, 6031–6046, https://doi.org/10.1002/joc.7166.

Stensrud, D. J., 1996: Importance of low-level jets to climate: A review. *J. Climate*, **9**, 1698–1711, https://doi.org/10.1175/1520-0442(1996)009<1698:IOLLJT>2.0.CO;2.

Su, L., 2023: Configurations of LLJs and associated rainfall patterns. Zenodo, accessed 7 September 2023, https://doi.org/10.5281/zenodo.8324895.

——, X. Sun, Y. Du, J. C. H. Fung, and G. Chen, 2023: The roles of local convergences in the convection initiation of a record-breaking rainfall event at the coastal Pearl River Delta in South China. *J. Geophys. Res. Atmos.*, **128**, e2022JD037234, https://doi.org/10.1029/2022JD037234.

Tang, W., J. Qin, K. Yang, F. Zhu, and X. Zhou, 2021: Does ERA5 outperform satellite products in estimating atmospheric downward longwave radiation at the surface? *Atmos. Res.*, **252**, 105453, https://doi.org/10.1016/j.atmosres.2021.105453.

Tu, C.-C., Y.-L. Chen, P.-L. Lin, and Y. Du, 2019: Characteristics of the marine boundary layer jet over the South China Sea during the early summer rainy season of Taiwan. *Mon. Wea. Rev.*, **147**, 457–475, https://doi.org/10.1175/MWR-D-18-0230.1.

——, ——, ——, and P.-H. Lin, 2020: The relationship between the boundary layer moisture transport from the South China Sea and heavy rainfall over Taiwan. *Terr. Atmos. Oceanic Sci.*, **31**, 159–176, https://doi.org/10.3319/TAO.2019.07.01.01.

Varuolo-Clarke, A. M., A. P. Williams, J. E. Smerdon, M. Ting, and D. A. Bishop, 2022: Influence of the South American low-level jet on the austral summer precipitation trend in southeastern South America. *Geophys. Res. Lett.*, e2021GL096409, https://doi.org/10.1029/2021GL096409.

Vera, C., and Coauthors, 2006: The South American low-level jet experiment. *Bull. Amer. Meteor. Soc.*, **87**, 63–78, https://doi.org/10.1175/BAMS-87-1-63.

Walters, C. K., and J. A. Winkler, 2001: Airflow configurations of warm season southerly low-level wind maxima in the Great Plains. Part I: Spatial and temporal characteristics and relationship to convection. *Wea. Forecasting*, **16**, 513–530, https://doi.org/10.1175/1520-0434(2001)016<0513:ACOWSS>2.0.CO;2.

Wang, L., W. L. Zhang, and J. Zhou, 2003: Statistic analysis on the south-westerly LLJ in China (in Chinese). *J. Nanjing Inst. Meteor.*, **6**, 797–805.

Wang, X., X. Dong, Y. Deng, C. Cui, R. Wan, and W. Cui, 2019: Contrasting pre-mei-yu and mei-yu extreme precipitation in the Yangtze River valley: Influencing systems and precipitation mechanisms. *J. Hydrometeor.*, **20**, 1961–1980, https://doi.org/10.1175/JHM-D-18-0240.1.

Wang, Z., Z. Wen, R. Chen, X. Li, and S. Huang, 2020: Interdecadal enhancement in the interannual variability of the summer monsoon meridional circulation over the South China Sea around the early 1990s. *Climate Dyn.*, **55**, 2149–2164, https://doi.org/10.1007/s00382-020-05375-3.

Whiteman, C. D., X. Bian, and S. Zhong, 1997: Low-level jet climatology from enhanced rawinsonde observations at a site in the southern Great Plains. *J. Appl. Meteor.*, **36**, 1363–1376, https://doi.org/10.1175/1520-0450(1997)036<1363:LLJCFE>2.0.CO;2.

Wu, G., S. Qin, Y. Mao, Z. Ma, and C. Shi, 2022: Validation of precipitation events in ERA5 to gauge observations during warm seasons over eastern China. *J. Hydrometeor.*, **23**, 807–822, https://doi.org/10.1175/JHM-D-21-0195.1.

Xia, R., and S. Zhao, 2009: Diagnosis and modeling of meso-β-scale systems of heavy rainfall in warm sector ahead of front in South China (middle part of Guangdong Province) in June 2005. *Chin. J. Atmos. Sci.*, **33**, 468–488, https://doi.org/10.3878/j.issn.1006-9895.2009.03.06.

Xia, R.-D., S.-X. Zhao, and J.-H. Sun, 2006: A study of circumstances of meso-β-scale systems of strong heavy rainfall in warm sector ahead of fronts in South China. *Chin. J. Atmos. Sci.*, **30**, 988–1008, https://doi.org/10.3878/j.issn.1006-9895.2006.05.26.

Xie, W., S. Yi, C. Leng, D. Xia, M. Li, Z. Zhong, and J. Ye, 2022: The evaluation of IMERG and ERA5-Land daily precipitation over China with considering the influence of gauge data bias. *Sci. Rep.*, **12**, 8085, https://doi.org/10.1038/s41598-022-12307-0.

Yanai, M., S. Esbensen, and J.-H. Chu, 1973: Determination of bulk properties of tropical cloud clusters from large-scale heat and moisture budgets. *J. Atmos. Sci.*, **30**, 611–627, https://doi.org/10.1175/1520-0469(1973)030<0611:DOBPOT>2.0.CO;2.

Zhang, M., and Z. Meng, 2019: Warm-sector heavy rainfall in southern China and its WRF simulation evaluation: A low-level-jet perspective. *Mon. Wea. Rev.*, **147**, 4461–4480, https://doi.org/10.1175/MWR-D-19-0110.1.

——, K. L. Rasmussen, Z. Meng, and Y. Huang, 2022: Impacts of coastal terrain on warm-sector heavy-rain-producing MCSs in southern China. *Mon. Wea. Rev.*, **150**, 603–624, https://doi.org/10.1175/MWR-D-21-0190.1.

Zhang, R., Y. Ni, L. Liu, Y. Luo, and Y. Wang, 2011: South China Heavy Rainfall Experiments (SCHeREX). *J. Meteor. Soc. Japan*, **89A**, 153–166, https://doi.org/10.2151/jmsj.2011-A10.

Zhang, W., H. Zhang, H. Liang, Y. Lou, Y. Cai, Y. Cao, Y. Zhou, and W. Liu, 2019: On the suitability of ERA5 in hourly GPS precipitable water vapor retrieval over China. *J. Geod.*, **93**, 1897–1909, https://doi.org/10.1007/s00190-019-01290-6.

Zhang, X., and Y. Ni, 2009: A comparative study of a frontal and a non-frontal convective systems. *Acta Meteor. Sin.*, **67**, 108–121.

Zhang, Y., C. Cai, B. Chen, and W. Dai, 2019: Consistency evaluation of precipitable water vapor derived from ERA5, ERA-Interim, GNSS, and radiosondes over China. *Radio Sci.*, **54**, 561–571, https://doi.org/10.1029/2018RS006789.

Zou, J., N. Lu, H. Jiang, J. Qin, L. Yao, Y. Xin, and F. Su, 2022: Performance of air temperature from ERA5-Land reanalysis in coastal urban agglomeration of Southeast China. *Sci. Total Environ.*, **828**, 154459, https://doi.org/10.1016/j.scitotenv.2022.154459.